Upper-ocean thermal variability controlled by ocean dynamics in the Kuroshio-Oyashio Extension region

Gyundo Pak, Young-Hyang Park, Frédéric Vivier, Romain Bourdallé-Badie, Gilles Garric, Kyung-Il Chang

AGU PUBLICATIONS

JGR

Journal of Geophysical Research: Oceans

RESEARCH ARTICLE

10.1002/2016JC012076

Upper-ocean thermal variability controlled by ocean dynamics in the Kuroshio-Oyashio Extension region

Gyundo Pak[1], Young-Hyang Park[2], Frédéric Vivier[2], Romain Bourdallé-Badie[3], Gilles Garric[3], and Kyung-Il Chang[1,4,5]

[1]School of Earth and Environmental Sciences, Seoul National University, Seoul, Korea, [2]Laboratoire LOCEAN-IPSL, Sorbonne Universités (UPMC, Univ. Paris 6)-CNRS-IRD-MNHN, Paris, France, [3]MERCATOR-OCEAN, Parc Technologique du Canal, Ramonville St. Agne, France, [4]Research Institute of Oceanography, Seoul National University, Seoul, Korea, [5]Now at GeoSystem Research Corporation, Gunpo, Korea

Key Points:
- The mechanisms of the upper-ocean KOE thermal variability are addressed from an eddy-resolving OGCM
- The observational evidence of increasing role of ocean dynamics since the 1990 regime shift is verified
- Decreased variability of surface heat flux after 1990 regime shift results in an increasing role of ocean dynamics

Correspondence to:
K.-I. Chang,
kichang@snu.ac.kr;
kichang@geosr.com

Citation:
Pak, G., Y.-H. Park, F. Vivier, R. Bourdallé-Badie, G. Garric, and K.-I. Chang (2017), Upper-ocean thermal variability controlled by ocean dynamics in the Kuroshio-Oyashio Extension region, *J. Geophys. Res. Oceans*, *122*, 1154–1176, doi:10.1002/2016JC012076.

Received 21 JUN 2016
Accepted 14 DEC 2016
Accepted article online 26 DEC 2016
Published online 15 FEB 2017

Abstract To understand the upper-ocean thermal variability in the Kuroshio−Oyashio Extension (KOE) region, the upper 400 m heat budget in the western North Pacific is analyzed for the 1981 − 2013 period using outputs from a high resolution (1/12°) ocean general circulation model. Winter heat storage rate on interannual to decadal time scales is mainly determined by oceanic heat advection rather than by net air-sea heat flux. The role of heat advection becomes particularly prominent and widely spread over the entire western North Pacific after the 1990 regime shift in association with the reduced variability of surface heat flux caused by weakened SST variability. The net heat flux acts to dampen temperature anomalies caused by the ocean dynamics. The ocean dynamics causing the upper-ocean heat storage rate is principally associated with the meridional shift of the Oyashio Extension front, which is significantly correlated with both the West Pacific and Pacific-North America teleconnection patterns.

1. Introduction

The western boundary of the North Pacific including the Kuroshio-Oyashio Extension (KOE) region has been known as the region where the ocean circulation is most variable in the North Pacific [*Nakamura et al*., 1997; *Qiu*, 2000] due to the inflow of the energetic Kuroshio and Oyashio. It is also a region where subsurface variability exerts a strong influence on sea surface temperature (SST), yielding the strongest decadal SST variability in the North Pacific [*Nakamura et al*., 1997], and where strong ocean-atmosphere interaction takes place [*Latif and Barnett*, 1994; *Seager et al*., 2001; *Schneider et al*., 2002; *Qiu et al*., 2007; *Kwon et al*., 2010; *Frankignoul et al*., 2011]. In contrast to the conventional extratropical ocean-atmosphere interaction characterized by atmospheric forcing on SST variations [*Cayan*, 1992], the SST forcing upon the overlying atmosphere is prevalent in the KOE region where ocean dynamics is very important [*Tanimoto et al*., 2003]. This ocean-to-atmosphere feedback occurs through vigorous turbulent heat fluxes, responsible for considerable oceanic heat release to the atmosphere especially in the boreal winter [*Sugimoto and Hanawa*, 2011], affecting the atmospheric boundary layer and storm track activity [*Nonaka and Xie*, 2003; *Tanimoto et al*., 2003]. These ocean-atmosphere interactions play an important role in generating interannual to decadal climate variability of ocean and atmosphere in local and remote regions in the North Pacific [*Kwon and Deser*, 2007; *Yamamoto and Hirose*, 2011; *Seo et al*., 2014]. Indeed, oceanic processes can induce interannual to decadal upper-ocean heat content variability in the KOE region [*Vivier et al*., 2002; *Kwon and Deser*, 2007], which in turn influence the atmosphere through the SST variability and resultant turbulent heat flux changes [*Tanimoto et al*., 2003].

The interannual to decadal SST variability in the North Pacific has been explained by the Pacific Decadal Oscillation (PDO) [*Mantua and Hare*, 2002] and the Victoria mode [*Bond et al*., 2003]; see also *Di Lorenzo et al*. [2008] for the North Pacific Gyre Oscillation (NPGO) which is the sea surface height (SSH) expression of the Victoria mode. *Yeh et al*. [2011] showed that a negative to positive PDO change, which is related to a strengthening of the Aleutian low and a warming of the tropical SST, is responsible for the winter North Pacific SST variability in the 1976/1977 regime shift. Also, the NPGO-like mode, which is the oceanic expression of the North Pacific Oscillation (NPO) [*Linkin and Nigam*, 2008] and West Pacific teleconnection pattern (WP) [*Wallace and Gutzler*, 1981; *Linkin and Nigam*, 2008], is shown to explain most of the SST variability in

the 1988/1989 regime shift. Another SST regime shift in the winter of 1998/1999 from a positive to a negative PDO change was reported [*Jo et al*., 2013]. An attempt was made by *An* [2008] to understand the chain of these long-term SST variability and regime shifts with a multidecadal oscillation mechanism associated with SST-zonal wind coupling and slow dynamic adjustment of the ocean. However, this multidecadal oscillation mechanism explains only long-term and basin-scale SST variability, but not so well interannual to decadal SST variations in the KOE region where oceanic variability and the ocean-atmosphere interaction are atypical and much stronger compared to the rest of the North Pacific. For example, unlike a direct atmospheric influence on the SST in the central and eastern North Pacific [*Cayan*, 1992], the SST variability of the KOE region reveals a lagged response by a few years to changes in atmospheric forcing, related to the PDO [*Qiu*, 2003] or WP/NPGO [*Sugimoto and Hanawa*, 2009; *Ceballos et al*., 2009] in the central North Pacific via westward propagating Rossby waves [*Miller et al*., 2004]. These results emphasize an important contribution of ocean dynamics to the KOE region thermal variability, although the degree of relative contribution of ocean dynamics as compared to the atmospheric influence has been shown to vary with epoch [*Kelly and Dong*, 2004; *Park et al*., 2012].

Attempts have been made to understand KOE SST variations on a variety of time scales. Seasonal SST changes are dominated by the net surface heat flux and entrainment from below the surface mixed layer [*Qiu and Kelly*, 1993; *Alexander et al*., 2000; *Vivier et al*., 2002]. On interannual to decadal timescales the KOE SST variability is associated with the latitudinal frontal shift [*Seager et al*., 2001; *Nonaka et al*., 2006] and changes in geostrophic advection [*Vivier et al*., 2002; *Taguchi et al*., 2007; *Kwon and Deser*, 2007; *Nonaka et al*., 2008] induced by the arrival of westward propagating baroclinic Rossby waves generated by wind stress curl forcing [*Deser et al*., 1999; *Schneider and Miller*, 2001; *Seager et al*., 2001; *Qiu*, 2003; *Qiu and Chen*, 2005; *Ceballos et al*., 2009; *Sugimoto and Hanawa*, 2009]. *Sugimoto and Hanawa* [2011] showed, based on satellite observations, a great influence of mesoscale anticyclonic eddies detached from the Kuroshio Extension (KE) on the KOE SST variability, although such a feature may represent the intrinsic frontal-scale dynamics superimposed on the broad-scale meridional structure generated by basin-wide wind forcing [*Taguchi et al*., 2007]. *Sugimoto and Hanawa* [2011] claimed that westward propagating Rossby wave signals and frontal displacement effects become greatly obscured by powerful eddy activity in the eddy-populated western boundary area west of 150°E. This is in line with the failure of the linear Rossby wave model hindcast in the westernmost KOE region by *Qiu* [2003], as previously remarked by *Park et al*. [2012].

Based on an extensive statistical analysis of observed SST and atmospheric variables in the western North Pacific, *Park et al*. [2012] evidenced an epoch-dependency of the dominant contributors to the KOE SST variability averaged over the area (142°−160°E, 35°−40°N). They found that, before 1990, the KOE SST variability was well correlated with the wind stress curl in the central/eastern basin of North Pacific at lags of 1, 3, and 4 yr, with the 3 − 4 year lags being suggestive of an influence of baroclinic Rossby wave propagation, consistent with previous works [*Deser et al*., 1999; *Schneider and Miller*, 2001; *Seager et al*., 2001; *Nonaka et al*., 2008]. After 1990, however, only the 1 yr lag correlation between the KOE SST and the central North Pacific wind stress curl was significant. The reason for this change in lags is still unclear. *Park et al*. [2012] regarded the 1 yr lagged signal of wind stress curl as the contribution of the ocean dynamics to the KOE SST, which then has changed significantly across the 1989/1990 regime shift, from a moderate contribution for 1970 − 1989 to a predominant contribution for 1990 − 2005. Recently, *Pak et al*. [2014] presented a nonstationary impact of atmospheric circulation on the SST variability in the western North Pacific: a strong influence during the strong winter monsoon period (1973 − 1987) and a significantly weakened impact during the weak monsoon period (1988 − 2002), indicating the epoch-dependency of main causes of the SST variability, consistent with *Park et al*. [2012]. Consequently, these results suggest that the ocean dynamics has played a central role for causing the decadal-scale SST variability in the western North Pacific after the abrupt decline of the East Asian Winter Monsoon (EAWM) around 1990.

SST is one of popular indicators to describe thermal state of the ocean because it is readily available, and it is also necessary to compute turbulent fluxes from the bulk flux algorithm [*Kelly and Dong*, 2004]. However, the upper-ocean heat content is a better climate predictor than SST for the ocean-to-atmosphere feedback [*Yulaeva et al*., 2001; *Kelly and Dong*, 2004; *Kelly et al*., 2010], in which the air-sea heat flux is a key parameter. While the evolution of the vertically integrated heat content down below a fixed depth is directly related to the air-sea heat flux (ignoring lateral processes), mixed layer temperature (MLT) variations depend also on changes in the mixed layer depth as well as the surface heat flux [*Dawe and Thompson*, 2007]. These

authors stressed that in contrast to a quick adjustment in the MLT budget, the heat content budget still shows significant variation for 4 years after the PDO shift, especially in the KOE region, thus is more appropriate for investigating climate-scale ocean-atmosphere interactions.

Despite a great number of previous studies, our present knowledge about the dynamics and causes of the interannual to decadal upper-ocean thermal variability in the KOE region remains limited and often debated as will be seen later. The observational subsurface data record is too short to investigate the upper-ocean heat budget at long time scales. We here instead resort to a realistic, 35 year long simulation from a high resolution ocean general circulation model (OGCM) to investigate the upper-ocean heat budget in the climatically important KOE region focusing on the regime-dependent thermal variability and its major causes, especially in the winter season when the ocean-atmosphere interaction is strongest.

The paper is organized as follows. Description of the high resolution OGCM data used in this study together with their validation are given in section 2. An upper-ocean heat budget analysis for two contrasting climate regimes that occurred before and after 1991 in the western North Pacific is given in section 3, with an emphasis on the wintertime thermal variability and negative feedback of ocean temperature in the KOE region. The major causes of the interannual to decadal scale variability of upper-ocean heat content in the KOE region are discussed in section 4, followed by a summary in section 5.

2. Data and Validation

2.1. OGCM and Model Products

A 35 year (1979–2013) simulation with a high resolution global OGCM is used to investigate interannual to decadal thermal variability in the KOE region. The model (referred to as ORCA12 hereafter) is based on the NEMO 3.5 [*Madec*, 2008] which is a framework of ocean related engines including ocean dynamics/thermodynamics, and sea-ice parts. The model solves the ocean primitive equations on C-grid system with hydrostatic and Boussinesq approximations. The presented ocean model has a 1/12° horizontal resolution operating on a tripolar ORCA grid type [*Madec and Imbard*, 1996; *Penduff et al*., 2010]. The ORCA12 grid delivers a horizontal resolution of 9.25 km at the equator, 7 km in midlatitude region, and 1.8 km in the Ross and Weddell Seas. The grid has 4,322 × 3,059 points in X and Y directions, respectively. The vertical grid has 75 levels of z-level coordinate with a grid space ranging from 1 m near the surface to 250 m at 5750 m. The topography is expressed with bottom partial cells [*Adcroft et al*., 1997; *Barnier et al*., 2006] using a combination of three databases: ETOPO1 [*Amante and Eakins*, 2009], GEBCO08 [*Becker et al*., 2009] merged for continental shelves shallower than 200 m, and Base 10 around the European coasts.

The total variance dissipation (TVD) formulation scheme, widely known as flux corrected transport scheme [*Boris and Book*, 1973], with anti-diffusive flux term is employed for the tracer advection. An energy and enstrophy conserving scheme [*Arakawa and Lamb*, 1981] is adopted for the momentum advection. To represent the exchange of the horizontal momentum and tracer due to the sub-grid scale processes, an isolevel-biLaplacian and a Laplacian-isopycnal diffusion schemes are employed, respectively. The K-epsilon scheme parameterizes vertical mixing coefficients. A partial-slip condition is applied for lateral boundary condition.

All the surface heat and momentum fluxes are calculated by bulk formula [*Large and Yeager*, 2004], using model-generated SST and meteorological variables such as wind vector, atmospheric temperature, relative humidity, and radiative/freshwater fluxes from ERA interim [*Dee et al*., 2011]. The time interval of flux data is daily superimposing diurnal cycle to the shortwave radiation, while the other atmospheric variables are subsampled at every 3 hours. The heat, freshwater, and momentum fluxes are modified in the presence of sea ice which is modeled by LIM2 sea ice model [*Bouillon et al*., 2009]. The monthly run-off climatology is built with data from *Dai and Trenberth* [2002].

The model run is performed from cold start with initial hydrographic data from January climatology [*Levitus et al*., 2005]. The temporal evolution of kinetic energy averaged over the upper 400 m in the western North Pacific region (140°−180°E, 28°−46°N) indicates that at least the upper 400 m of the model has reached equilibrium since the end of 1980, with the area-mean kinetic energy fluctuating around a constant value of 0.023 $m^2\ s^{-2}$ (Figure 1). Hence, the first 2 year integration is considered as a spin-up period, and we analyzed 3 day averaged outputs for the last 33 years (1981 − 2013).

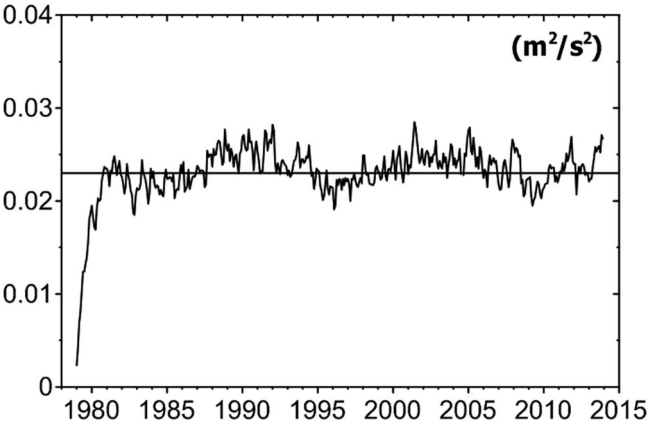

Figure 1. Temporal evolution of volume-averaged kinetic energy (unit is $m^2\ s^{-2}$) over the upper 400 m in the western North Pacific (140°−180°E, 28°−46°N) obtained from monthly averaged horizontal velocities. A solid line indicating constant value of 0.023 $m^2\ s^{-2}$ is overlaid.

Although the model was integrated globally, our domain of analysis is mostly limited in the western North Pacific (140°−180°E, 28°−46°N). To obtain a representative area-averaged time series, the KOE region is selected as the region (150°−165°E, 36°−42°N) corresponding to the primary center of the upper-ocean thermal variability, as will be clear later in section 4. Our KOE region corresponds to a very similar place as in previous studies based on observational data such as *Tanimoto et al.* [2003] (140°−165°E, 35°−45°N) and *Park et al.* [2012] (142°−160°E, 35°−40°N). In our case, the region west of 150°E was excluded due to the prevalence of mesoscale activity which obscures large-scale upper-ocean thermal variability caused by basin-scale atmospheric forcing [*Sugimoto and Hanawa*, 2011]. The KOE region lies approximately between the KE (along 36°N in ORCA12) and the Oyashio Extension (OE, along 41°N in ORCA12) (Figure 2), and corresponds to the mixed water region according to *Qiu* [2001]. The results of subsequent analyses are not so sensitive to the different selection of the KOE region within a few degrees in longitudes or latitudes.

The model has ocean-only component without any data assimilation and coupling with atmospheric models, and it provides dynamically-consistent continuous three-dimensional physical fields with a long time span.

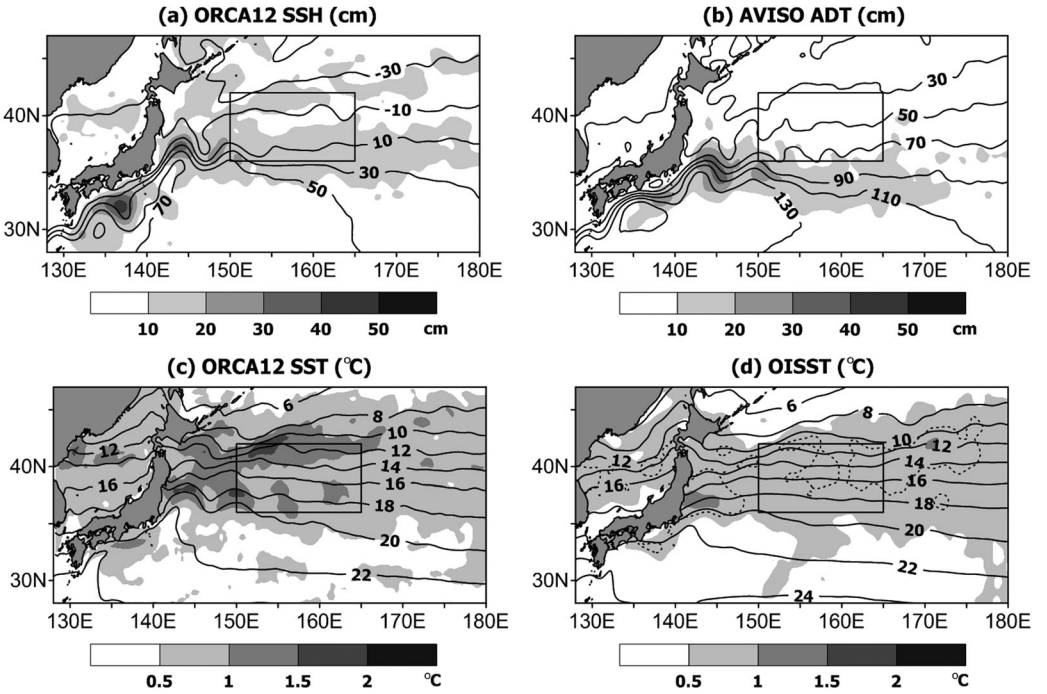

Figure 2. Climatological mean (1993 − 2013) SSH from (a) ORCA integration and (b) AVISO ADT. Contour interval is 20 cm. Climatological mean (1982 − 2013) SST from (c) ORCA integration and (d) OISST. Contour interval is 2°C. Standard deviations of annual averaged are marked as shading. (d) Dotted lines indicate standard deviation of 0.75°C. The rectangular domain (150°−165°E, 36°−42°N) indicated in (a)∼(d) is used for defining the KOE region.

2.2. Model Validation

The ORCA12 SSH and SST are compared with the daily 1/4° gridded absolute dynamic topography (ADT) product distributed by Archiving, Validation, and Interpretation of Satellite Oceanographic data (AVISO, http://www.aviso.altimetry.fr./duacs/) and the version 2 of the optimally interpolated 1/4° daily AVHRR (Advanced Very High Resolution Radiometer) derived SST (OISST) [*Reynolds et al*., 2002]. We consider the ORCA12 MLT as its SST, because both MLT and SST are frequently used interchangeably [*Grodsky et al*., 2008]. Indeed, the temporal variability of MLT is almost same as that of the model's temperature at the first z-level (not shown). Comparison periods are 1993 − 2013 for SSH and 1982 − 2013 for SST, considering overlapping periods between ORCA12 and other data sets. Note that the comparison period for winter (December-February) interannual variability of SSH (Figures 3e) is set to 1994 − 2013 because the daily ADT in December 1992 is not provided. Similarly, comparison period for winter SST is also limited to 1983 − 2013 (Figure 3f). Here the winter SST (or SSH) of 1994 refers to the mean SST (or SSH) during December 1993 to February 1994. The interannual standard deviation (shading in Figure 2) is calculated from annual mean SSH and SST fields of both ORCA12 and satellite data sets.

2.2.1. Spatial Distribution

The record-length (1993 − 2013) mean SSH field of ORCA12 (Figure 2a) reproduces well the major features of KE seen in AVISO ADT (Figure 2b) such as two quasi-stationary meanders locating near 144°E and 150°E [*Qiu and Chen*, 2005]. Model-data discrepancies include model's overshooting of the Kuroshio by about 1° northward and stronger meander south of Japan (137°E, 32°N). The record-length (1982 − 2013) mean ORCA12 SST field (Figure 2c) also shows a spatial distribution similar to that of OISST (Figure 2d). Note that

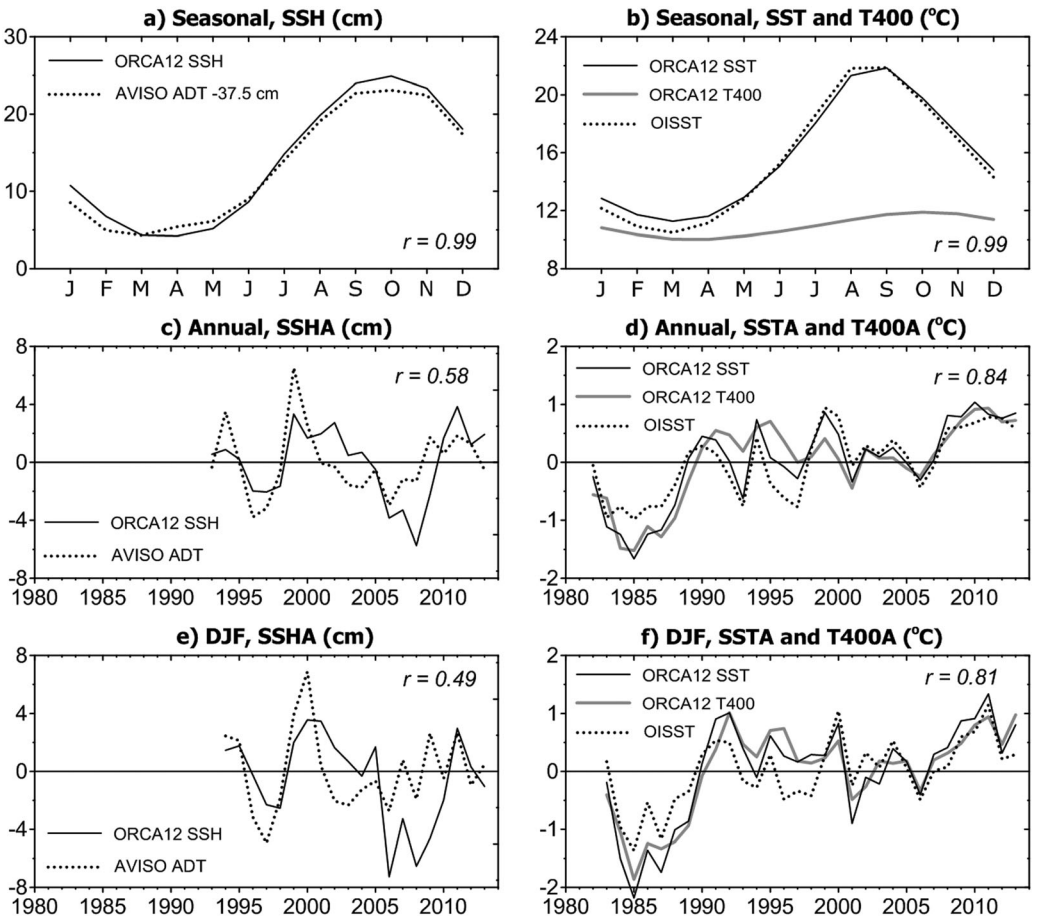

Figure 3. Time series of (a, c, e) SSH and (b, d, f) SST averaged over the KOE region shown in Figure 1, from ORCA simulation (solid lines) and observations (dotted lines) (AVISO ADT for SSH and OISST for SST). Temporal evolution of T400 is also overlaid in (b, d, f) with gray lines. (a−b) Monthly climatologies, (c−d) annual mean anomalies, and (e−f) winter (December–February) mean anomalies. Correlation coefficients presented in each figure indicate those between observations and ORCA12 surface variables (SSH or SST).

the original ORCA12 variables have been averaged and resampled in a 0.25° by 0.25° grid, consistent with the horizontal grid spacing of AVISO ADT and OISST.

The spatial distribution of interannual variability (shading) is also well reproduced by ORCA12 especially for SSH (Figures 2a and 2b). The interannual variability of SSH is large along the KE, and particularly enhanced (>30 cm RMS) for the western quasi-stationary meander centered at (144°E, 35°N) in both ORCA12 SSH and AVISO ADT. The region south of Japan also shows relatively strong interannual variability for both ORCA12 SSH and AVISO ADT. The interannual variability south of Japan, however, is much greater (>40 cm) in ORCA12 SSH than that of AVISO ADT (~25 cm). This is related to the vigorous spatial variability of the warm eddy-like features south of Japan in the ORCA12, while it is relatively stable in AVISO ADT. The ORCA12 SSH shows also higher temporal variability compared to that of the AVISO ADT just north of 40°N where the OE is generally located [*Frankignoul et al*., 2011].

Both ORCA12 SST and OISST show the strongest interannual variability greater than 0.5°C in the latitude band between 35°N and 45°N comprising the KE and OE. The interannual variability of ORCA12 SST is generally higher than that of OISST west of 165°E, with the strongest variability concentrated along the OE centered at 41°N and to a lesser extent along the KE centered at 36°N in ORCA12 (Figures 2c and 2d). The most noticeable discrepancy in SST variability is observed north of 40°N especially along the OE (~1.5°C) where OISST shows much weaker variability (~0.8°C), although the OE region in OISST also shows enhanced variability (dotted lines in Figure 2d) compared to other regions in the domain.

2.2.2. Seasonal and Interannual Variations

To examine the temporal variability of ORCA12 SSH and SST in more detail, time series of spatially-averaged SSH and SST in the KOE region are presented in Figure 3. The seasonal cycle of ORCA12 SSH and SST has a good agreement with that of AVISO ADT and OISST (Figures 3a and 3b), both in terms of amplitude and phase, with a correlation coefficient exceeding 0.99. Note that −37.5 cm is added to the seasonal variability of AVISO ADT to fit the range of ORCA12 SSH because it is difficult to compare the absolute value of SSH due to the difference in the reference levels for ORCA12 SSH and AVISO ADT. The seasonal cycle of ORCA12 SST is almost the same as that of OISST except for a warm bias of 0.5°C in ORCA12 SST during cold season (January-March). ORCA12 T400 (depth-averaged temperature from surface to 400 m) also shows seasonal variability with a lag of one month compared to seasonal variability of SST, so that T400 shows maximum and minimum on October (11.9°C) and April (10.0°C), respectively.

The interannual variability shown in Figure 3c is based on the annually-averaged monthly anomalies that are obtained after removing the monthly climatology. We note that the ORCA12 SSH shows a decreasing trend (not shown), which is not observed in the AVISO ADT (Figure 2c), suggesting that the deeper layer of the model below 400 m is far from equilibrium during the analysis period in contrast to the upper 400 m. In the subsequent analyses, this model drift is removed by detrending the original ORCA12 SSH time series. The detrended ORCA12 SSH and AVISO ADT are moderately correlated with each other at 0.58 for annual means (Figure 3c) and at 0.49 for winter means (Figure 3e), but both are significant at the 99% confidence level, indicating that the interannual SSH variability is reasonably well reproduced in ORCA12. The interannual variability of ORCA12 SST shows a far better agreement with OISST for both annual means ($r = 0.84$, Figure 3d) and winter means ($r = 0.81$, Figure 3f). These results indicate that one can confidently use the ORCA12 outputs for investigating the upper-ocean thermal variability in the western North Pacific. The variability of T400 also agrees well with that of SST for annual ($r = 0.81$, Figure 3d) and winter ($r = 0.93$, Figure 3f) average.

2.3. Ancillary Data and Correlation Analysis

In order to document the relationship between the ocean dynamics in the ORCA12 and the overlying atmospheric circulation patterns, the indices of the winter WP and Pacific-North America (PNA) teleconnection patterns are obtained from the web site of the NOAA Climate Prediction Center (http://www.cpc.ncep.noaa.gov/).

Most of the subsequent analyses are based on the linear correlation coefficients, which are obtained after removing linear trends of each annual time series. The significance level of 95% is used to test all correlation coefficients, unless otherwise stated. The confidence limit of the correlation coefficient is obtained based on two tailed *t*-test with effective degree of freedom which is estimated by dividing the data length by the integrated product of normalized autocovariances of each time series [*Emery and Thomson*, 1997]. Also, the

difference of two given standard deviation (variance) is tested using F distribution with N-1 (N: data length) degree of freedom and 95% significance level.

3. Heat Budget of the Upper 400 m

3.1. Heat Budget Equation

The governing equation for potential temperature T in the ocean neglecting horizontal diffusion is,

$$\frac{\partial T}{\partial t} = \frac{1}{\rho c_p}\frac{dq}{dz} - \boldsymbol{u}\cdot\nabla T - w\frac{\partial T}{\partial z} + \frac{\partial}{\partial z}\left(\kappa\frac{\partial T}{\partial z}\right), \tag{1}$$

where $\boldsymbol{u}$ (u, v) and w are the horizontal and vertical velocities, respectively, κ is the vertical eddy diffusivity, and q is the radiative heating. The specific heat at constant pressure c_p is set in the model to a fixed value as 4000 J kg^{-1}°C^{-1}. The potential density ρ is considered as a constant (=1035 kg m^{-3}) in subsequent analyses as it changes by less than 2% for the range of T and salinity in the KOE region, although the model uses the nonlinear equation of state.

Integrating (1) from a fixed depth (h = *400 m*), a depth deeper than the winter mixed layer, to the surface yields

$$\frac{\partial}{\partial t}\int_{-h}^{0} T dz = \frac{Q_{rad}}{\rho c_p} - \int_{-h}^{0}\boldsymbol{u}\cdot\nabla T dz - \int_{-h}^{0} w\frac{\partial T}{\partial z}dz + \int_{-h}^{0}\frac{\partial}{\partial z}\left(\kappa\frac{\partial T}{\partial z}\right)dz, \tag{2}$$

where Q_{rad} is the radiative heat flux at the surface and the penetration of the short wave radiation below h is neglected. The 400 m depth for h has been chosen because it is sufficiently deep to cover the deepest winter mixed layers (100 − 200 m) and at the same time corresponds to the representative thermocline depth in the KOE region. In addition, it is well below the penetration depth of the short-wave radiation [*Hosoda et al*., 2015]. Dividing by h and extracting the surface turbulent flux $\left(\kappa\frac{\partial T}{\partial z}\right)_{z=0}$ from the last term of the right-hand-side (rhs) of (2), we obtain a tendency equation for the vertically averaged temperature of the upper 400 m water column, denoted by T400:

$$\frac{\partial T400}{\partial t} = \frac{Q_{net}}{\rho c_p h} - \frac{1}{h}\int_{-h}^{0}\boldsymbol{u}\cdot\nabla T dz - \frac{1}{h}\int_{-h}^{0} w\frac{\partial T}{\partial z}dz - \frac{1}{h}\left(\kappa\frac{\partial T}{\partial z}\right)_{z=-h}, \tag{3}$$

where Q_{net} is the net surface heat flux, sum of the surface radiative and turbulent fluxes. Our final form of the heat budget equation is expressed in flux form (W m^{-2}) by multiplying $\rho c_p h$,

$$\frac{\partial(HC)}{\partial t} \equiv \mathrm{HSR} = Q_{net} - \rho c_p\int_{-h}^{0}\boldsymbol{u}\cdot\nabla T dz - \rho c_p\int_{-h}^{0} w\frac{\partial T}{\partial z}dz, \tag{4}$$

where HC ($=\rho c_p h T400$) is the upper 400 m heat content, and we have further neglected the small vertical diffusion term at 400 m $-\frac{1}{h}\left(\kappa\frac{\partial T}{\partial z}\right)_{z=-h}$. This equation (4) states that the heat storage rate (HSR) or the temporal variation of heat content in the upper 400 m is the sum of the net surface heat flux Q_{net} and integrated horizontal heat advection HADV (second rhs term) and vertical heat advection VADV (third rhs term). Here, the total heat advection ADV (= HADV + VADV) is calculated from the TVD scheme, the same scheme used in the model, with the model's three-dimensional temperature and velocity fields. VADV is also separately calculated by one-dimensional centered scheme. HADV is then calculated by subtracting VADV from ADV. A positive (negative) Q_{net} means oceanic heat gain (release). Since only 3 day averaged fields of ORCA12 are available, the contributions of HADV and VADV with time scales shorter than 3 days are unresolved. These unresolved high-frequency heat advection together with horizontal and vertical diffusion terms are considered as a residual. All the heat budget terms are monthly averaged after calculating them with 3 day fields. It is to be noted that neglecting residual term affects little the major conclusion of the present study because the difference between HSR and the sum of Q_{net} and ADV is insignificant, as shown later. There is, however, one exception to this in August 2004 when there appears an abnormal feature in HADV due to the presence of erroneous horizontal velocities in the model outputs for unknown reasons. These erroneous data in August 2004 have been discarded when analyzing seasonal heat budget, interannual summertime (June-August) variability, and annual-mean HADV. However, it affects little interannual wintertime (December−February) variability that is our major interest.

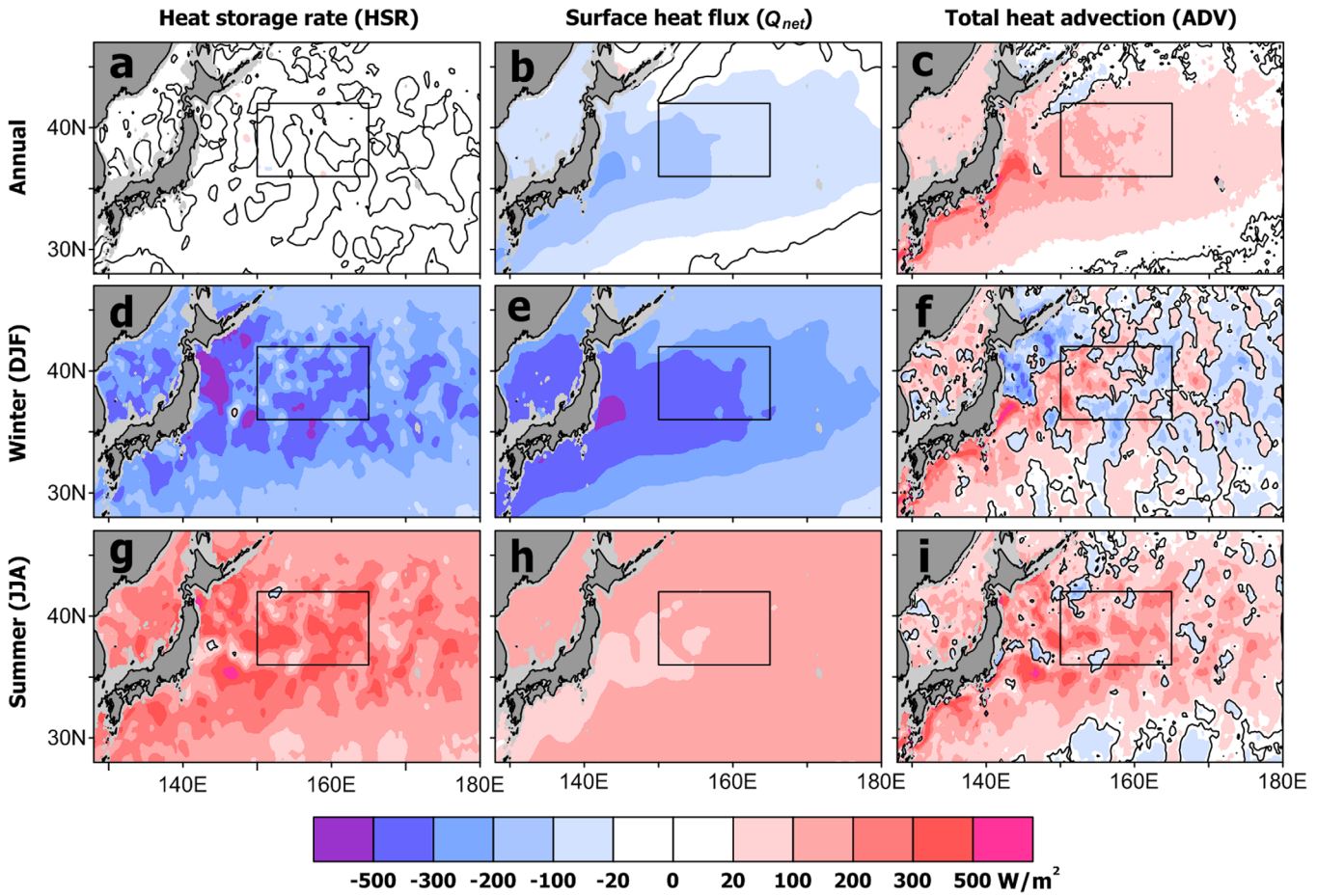

Figure 4. Spatial distribution of (a, d, g) heat storage rate (HSR), (b, e, h) net surface heat flux (Q_{net}), and (c, f, i) heat advection (ADV). (a−c) Annual mean, (d−f) winter mean, and (g−i) summer (June–August) mean.

3.2. Mean and Seasonal Variation

Figure 4 shows the spatial distribution of record-length (1981 − 2013) mean heat budget terms averaged on a grid of 0.25°×0.25°. The long-term mean annual HSR (Figure 4a) is almost zero throughout the domain, indicating that the net surface heat flux (Q_{net}, Figure 4b) and the total heat advection ADV (HADV + VADV; Figure 4c) nearly exactly counterbalance each other with a maximum magnitude of about ±200 W m^{-2} along the Kuroshio and KE. If ADV is divided into HADV and VADV, the two terms have similar magnitudes but opposite signs along the quasi-stationary meanders of KE (Figure 5). The energetic VADV along the KE appears to be due to vertical motions associated with the Kuroshio meander [*Sainz-Trapaga and Sugimoto*, 2000]. Although the contribution of VADV is not negligible in the energetic Kuroshio and KE region where nonlinear dynamics is expected to be important, ADV outside of these highly energetic regions is dominated primarily by HADV especially in the KOE region (compare different panels in Figure 5). As we are principally interested in the KOE region and in order to focus on the comparative analysis between two dominant forcing factors, Q_{net}-related atmospheric forcing and ADV-associated ocean dynamics, we will mainly compare Q_{net} with ADV rather than splitting ADV into HADV and VADV.

The winter (December−February) HSR is negative throughout the study area (Figure 4d), indicating that heat is systematically released from the ocean to the atmosphere with the greatest magnitude lying between 33°N and 42°N, a band comprising the KE, OE, and KOE region (KE−OE band hereafter). The overall large-scale pattern of HSR resembles Q_{net} (Figure 4e), while its small scale features are mostly due to ADV (Figure 4f). Negative ADV found along the east coast of Japan north of 35°N in winter (Figure 4f) is not observed during summer (June−August) when ADV contributes positively to the heat budget in most parts of the domain (Figure 4i). The seasonal variation of ADV in the northeastern coastal region of Japan is

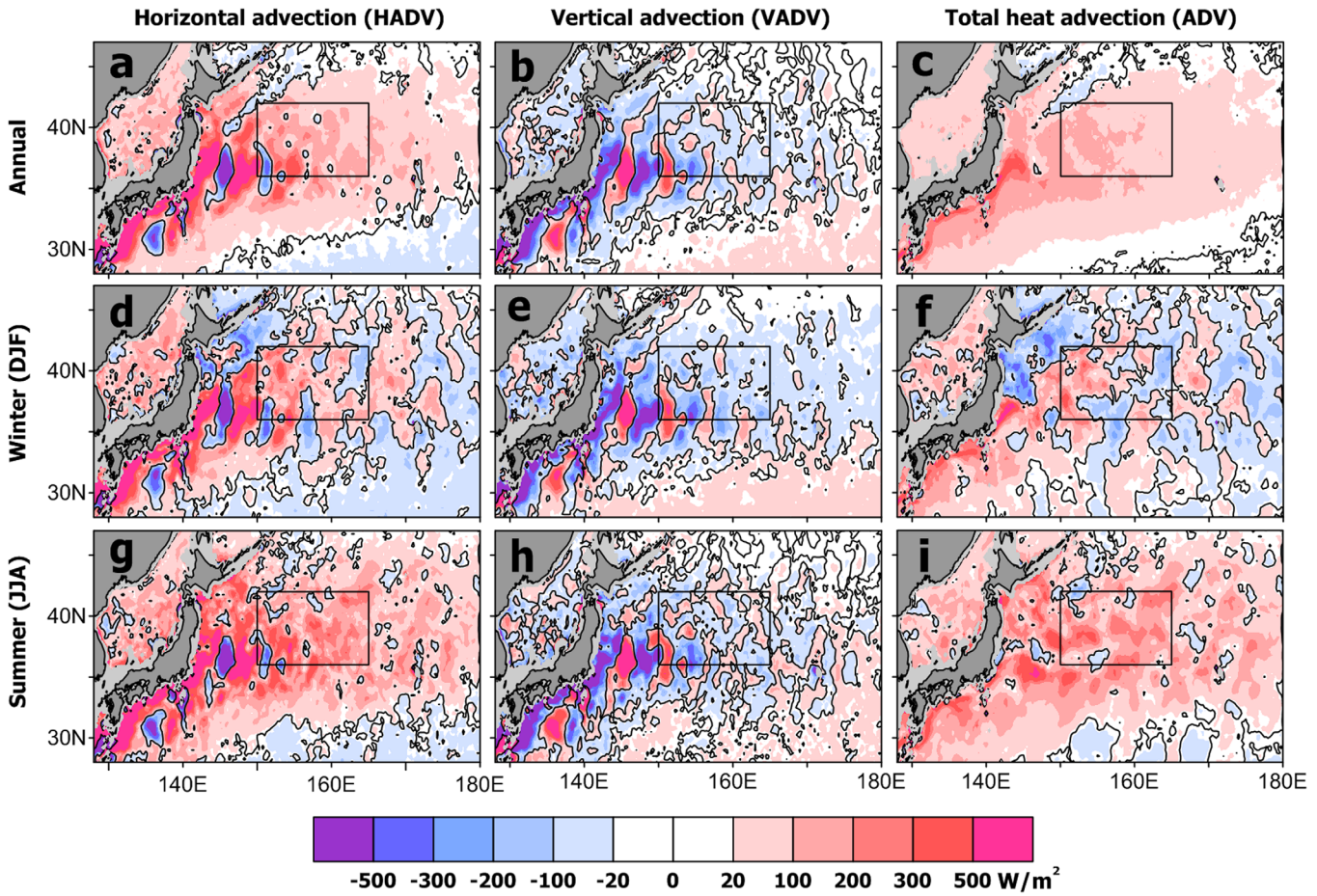

Figure 5. Spatial distribution of (a, d, g) horizontal (HADV) and (b, e, h) vertical (VADV) heat advection terms as well as (c, f, i) their sum (ADV). (a-c) Annual mean, (d-f) winter mean, and (g-i) summer mean.

mainly due to HADV (Figures 5d and 5g), because the seasonality of VADV is not apparent (Figures 5b, 5e, and 5h). This suggests that the negative ADV in the northeastern coast of Japan in winter (Figure 5f) is due to the cold water advection by the Oyashio, in agreement with *Tatebe and Yasuda* [2005]. It is interesting to note that the spatial distribution of the summertime Q_{net} (Figure 4h) nicely depicts the geographical location occupied by the Kuroshio/KE system, revealing a band of slightly lower Q_{net} compared to surrounding areas. This may indicate that warm Kuroshio waters tend to damp Q_{net} probably due to enhanced upward turbulent fluxes caused by comparatively higher SST than surroundings, thus partly compensating dominant downward radiative heat fluxes.

As Q_{net} varies over far larger spatial scales compared to ADV containing substantial mesoscale variability (see Figure 4), all the heat budget components in subsequent analyses are spatially smoothed with a window size of 6°×4°, designed to suppress the mesoscale eddies, mean diameter of which is about 160 km (maximum diameter about 280 km) [*Cheng et al*., 2014], unless otherwise stated. In Figure 6, the seasonal variations of the heat budget terms are displayed in time-latitude plots, where the monthly terms are zonally averaged between 150°E and 165°E over the longitudinal range of the KOE region. The seasonal cycle of all heat budget terms is most pronounced in the KE−OE band as in *Vivier et al*. [2002], although their study only covers regions south of 38°N. The seasonal cycle of HSR (Figure 6a) closely resembles the Q_{net} cycle, with the nearly same magnitude in winter (Figure 6b) because of the negligible contribution from ADV (Figure 6c). However, the contribution from ADV becomes increasingly important in summer, with its magnitude being comparable to or even exceeding Q_{net} (Figure 6c). In the KE−OE band (33°−42°N), HADV with positive heat transport forms a major contributor to ADV (Figure 6d). In contrast, VADV shows generally negative heat transport regardless of seasons except in September to November, and mostly counterbalances HADV during

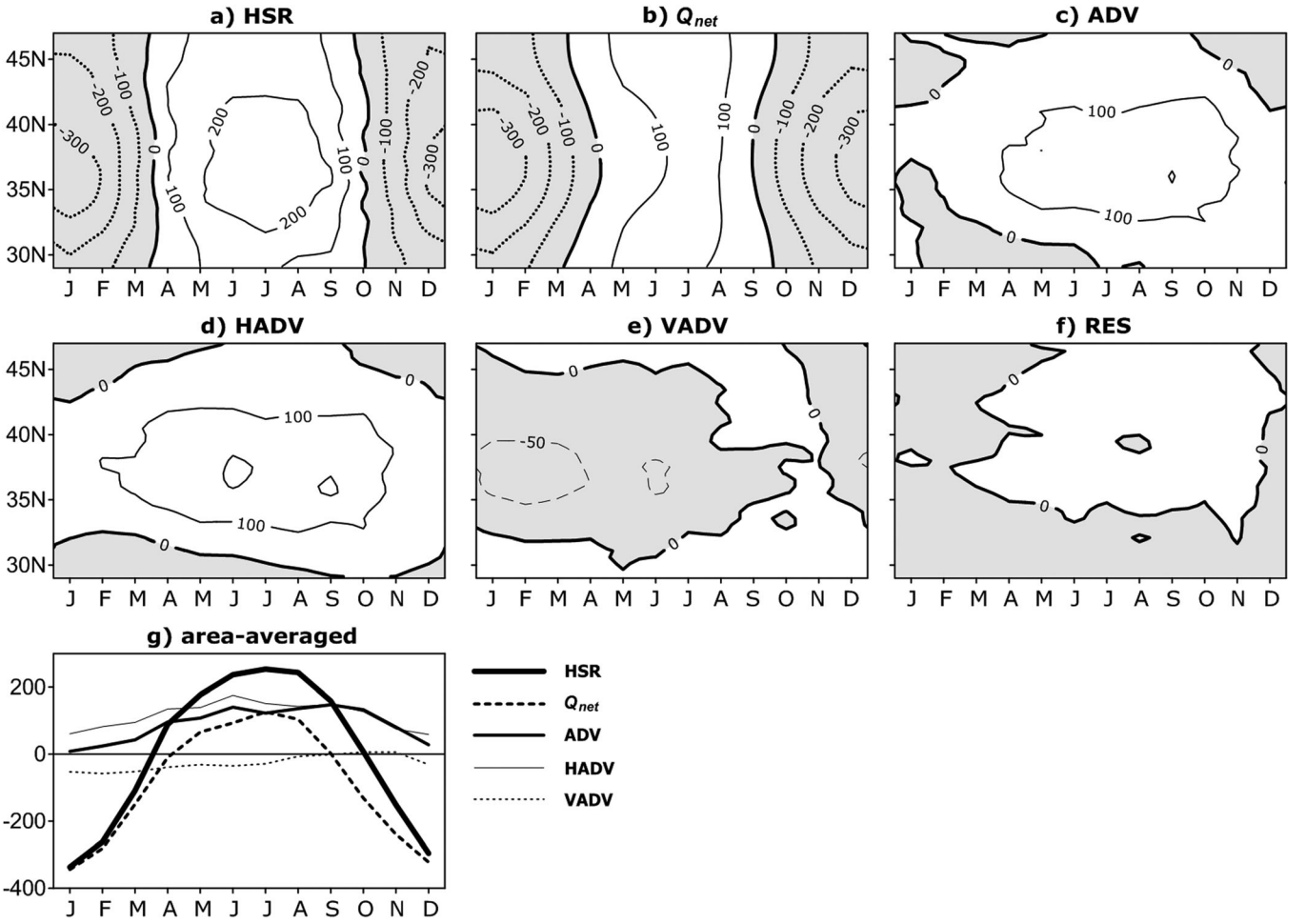

Figure 6. Zonal mean (150°–165°E) seasonal climatologies of (a) heat storage rate (HSR), (b) net heat surface flux (Q_{net}), (c) total heat advection (ADV), (d) horizontal heat advection (HADV), (e) vertical heat advection (VADV), and (f) residual (RES) over the western North Pacific between 28°N and 46°N. Model outputs have previously been spatially smoothed with a 6°×4° window. Contour interval is 100 W m^{-2} and supplementary contour of −50 W m^{-2} is added in (e). Negative values are shaded. (g) Spatially averaged monthly climatologies of heat budget components (in W m^{-2}) in the KOE region (150°−165°E, 36°−42°N).

the cold season (January−March) (Figure 6e). The residual RES, which is the difference between the HSR and sum of ADV and Q_{net}, shows a minor influence of only ±10 W m^{-2} at most (Figure 6f), indicating that the heat budget equation (4) is well closed by Q_{net} and ADV.

The area-averaged Q_{net} in the KOE region is strongly negative in cool seasons (October−March) with a peak close to −340 W m^{-2} in January, while it is positive during warmer seasons (May−September) with a peak at about 120 W m^{-2} in July, yielding a net heat loss of 90 W m^{-2} to the atmosphere on an annual average (Figure 6g). The latter value is comparable with those documented in previous works [*Qiu and Kelly*, 1993; *Moisan and Niiler*, 1998]. This net heat loss by Q_{net} is largely compensated by ADV, which is dominated by HADV. The area-averaged ADV in the KOE region contributes positively to HSR throughout the year with a maximum of about 150 W m^{-2} in September, but it is close to zero during the winter season. A plausible explanation for this minor contribution of wintertime ADV may be attributed to the enhanced cold advection by the southward flowing Oyashio and local Ekman transport (not shown), largely counterbalancing warm advection by the Kuroshio system. Consequently, HSR, which is nearly equal to the sum of Q_{net} and ADV, shows strong seasonal variability, with its sign changing from negative to positive in April and from positive to negative in October, yielding a minimum T400 in April and a maximum T400 in October as shown in Figure 3b.

3.3. Winter Heat Budget in the KOE Region for Two Contrasting Epochs

Although our focus is to investigate interannual to decadal variability of the winter upper-ocean temperature (heat content), we first discuss the heat budget in terms of annual anomalies since the decadal SST

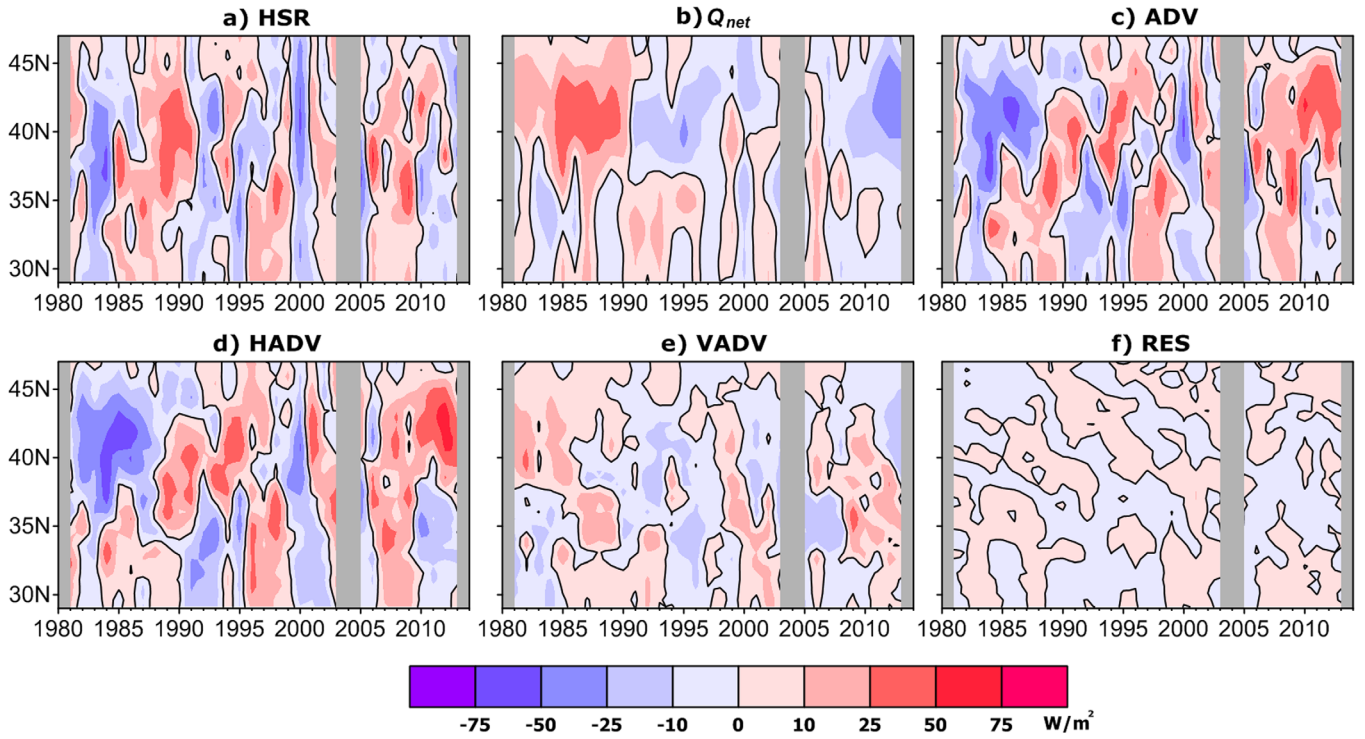

Figure 7. Zonal mean (150°−165°E) annual anomalies of (a) heat storage rate (HSR), (b) net surface heat flux (Q_{net}), (c) total heat advection (ADV), (d) horizontal heat advection (HADV), (e) vertical heat advection (VADV), and (f) residual (RES) over the western North Pacific between 28°N and 46°N.

variability is influenced by the evolution of HSR during the entire year [*Tomita et al.*, 2002]. Annual mean nonseasonal anomalies of heat budget terms are obtained by removing their monthly climatology and averaging from January of the present year to the following January. Latitude-year maps of zonally averaged (150°−165°E) anomalies of heat budget terms are shown in Figure 7. Each term is computed from spatially smoothed (window size of 6°×4°) fields and the data of year 2004 are discarded for the reason already mentioned. Nonseasonal anomalies of Q_{net} and ADV in the KOE region before 1990 are comparable in magnitude, especially between 38°N and 44°N within and slightly north of the KOE region. However, ADV anomalies afterward are much larger compared to Q_{net} anomalies and well correlated with HSR anomalies (Figures 7a−7c). Q_{net} anomalies north of 36°N corresponding to the model KE latitude shows an opposite tendency of temporal variability compared to those south of 36°N. This is one of the reasons why we have selected KOE region to the north of 36°N to exclude the Kuroshio recirculation region south of 36°N. The ADV variability is dominated by HADV (Figure 7d), whereas VADV (Figure 7e) shows significantly weaker variability at all latitudes considered, with mostly an opposite sign to HADV. Note that the Ekman heat transport has insignificant contribution to the HADV in the interannual to decadal time scale in this region (not shown), consistent with *Kwon and Deser* [2007]. The residual RES (Figure 7f) is negligible compared to HSR and ADV especially in the KOE region, indicating that the heat budget balance equation (4) is reasonably well closed for nonseasonal variations.

Time series of area-averaged annual and winter anomalies of HSR, Q_{net}, and ADV in the KOE region show that the interannual variability of HSR can be mostly explained by ADV during the entire study period (Figures 8a and 8b), consistent with previous studies [*Vivier et al.*, 2002; *Kwon and Deser*, 2007]. Compared to the ADV variability, Q_{net} shows a significant decreasing trend, which makes the interdecadal change prominent rather than interannual variations. In fact, the Q_{net} variation is characterized by large positive anomalies (+35 W m^{-2}) during the 1980s and weakly negative anomalies (−10 W m^{-2}) until 2008. This interdecadal difference (45 W m^{-2}) dominates over the relatively weaker interannual signals (17 W m^{-2}). Since 2008, Q_{net} decreases continuously until the end of the analysis period, indicative of enhanced oceanic heat transfer to the atmosphere in recent years. Similar interannual to decadal variability of the KOE Q_{net} is also observed from other data sets such as OAFlux [*Yu et al.*, 2008] and NCEP reanalysis 1 [*Kalnay et al.*, 1996]

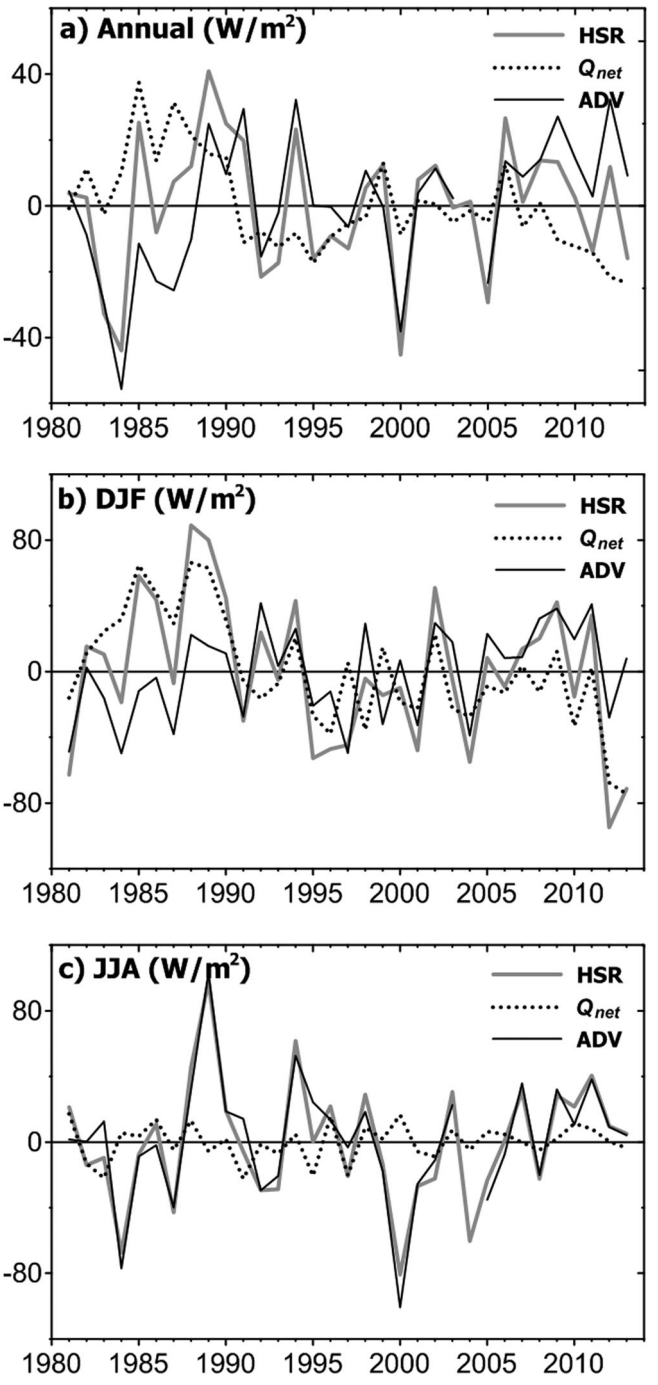

Figure 8. KOE region-averaged anomalies of HSR (thick solid lines), Q_{net} (dotted lines), and ADV (thin solid lines). (a) Annual mean, (b) winter (DJF) mean, and (c) summer (JJA) mean.

(Figure 9). When Q_{net} has large positive anomalies at the end of the 1980s, the relationship between HSR and ADV is noticeably weaker especially in the winter during the 1980s, as compared to that after 1991 when the two heat budget terms are tightly correlated (Figures 8a and 8b).

Based on this observation of different contributions of Q_{net} and ADV to HSR variations, we have divided the analysis period into three contrasting epochs: 1981 − 1990, 1991 − 2008, and after 2008. The first two periods, which are considered here as our two contrasting epochs, correspond to two different climate regimes described in *Park et al.* [2012] and *Pak et al.* [2014], although the regime shift from the strong EAWM (1973 − 1987) to the weak EAWM (1988–2002) in *Pak et al.* [2014] occurs 3 years earlier than the shift described here (1990/1991). This epoch-dependent difference in the relative contribution of forcing factors to KOE HSR variations has been observed only in winter and annual mean anomalies (Figures 8a and 8b), while summer anomalies show the predominance of ADV over the entire analysis period (Figure 8c). This indicates that the epoch-dependent contrasting variability is most apparent in the winter season when the air-sea turbulent heat flux is most vigorous and the surface mixed layer is deepest.

The temporal standard deviations of Q_{net} and ADV in the KOE region are 48.0 W m^{-2} and 27.7 W m^{-2}, respectively, during E1 period (1981 − 1990), suggesting that relatively stronger influence of Q_{net} to HSR compared to that of ADV. On the other hand, during E2 period (1991 − 2008), the standard deviations of KOE Q_{net} and ADV are 19.4 W m^{-2} and 27.4 W m^{-2}, respectively. This change of temporal standard deviation of two heat budget terms is consistent with the observation above mentioned that the relationship between HSR and Q_{net} is stronger during E1 period while HSR and ADV are tightly correlated to each other during E2 period. Detail description of the epoch-dependent contribution of each heat budget term will be given in section 4.3.

These ORCA12 model-derived results are consistent with *Park et al.* [2012] who evidenced from observational data the importance of ocean dynamics in determining the winter KOE SST and its increasingly important role during the weak EAWM period (1990 − 2005) compared to the strong EAWM period (1970 − 1989). *Pak*

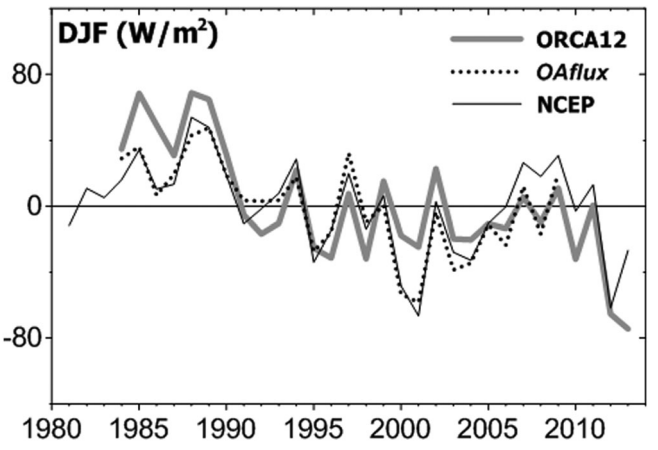

Figure 9. Comparison of time series of winter KOE Q_{net} in W m^{-2} from various data sources such as ORCA12 (gray), OAflux [*Yu et al*., 2008] (dotted), and NCEP reanalysis 1 [*Kalnay et al*., 1996] (black solid).

et al. [2014] also showed a regime-dependent nonstationary impact of the atmospheric circulation represented by the EAWM and NPO on the winter SST in the western North Pacific. They showed that during the strong EAWM regime (1973 – 1987), which matches well our E1 period, both atmospheric indices are well correlated with the late winter SST in the western North Pacific with a lag of one month, while the correlation decreases significantly during the weak EAWM regime (1988 – 2002), a period also close to our E2 period. However, a closer look at the KOE region reveals that the winter KOE SST variability is not well explained by EAWM and NPO indices [see *Pak et al*., 2014, Figure 2] in both strong and weak EAWM epochs.

Although the contribution to HSR of both ADV and Q_{net} changes with the monsoon epochs, the monsoon intensity cannot be directly ascribed to the main contributor to the SST variability (HSR). Especially, the winter Q_{net} anomalies show positive values in the E1 period (Figure 8b) indicating counter-intuitively less wintertime heat loss to atmosphere during the strong EAWM period. Further discussion is given in section 4.2.

4. Possible Mechanisms for Interannual to Decadal Q_{net} and ADV Variability

4.1. Upper Ocean Thermal Variability Due to the Meridional Shifts of Oceanic Fronts

Figure 10 shows two leading EOFs and corresponding PCs of T400 in the western North Pacific. The EOF1 (Figure 10a) explains 52% of the total variance, with the same sign for the entire domain. The KOE region lies in the region of the strongest variability, and indeed the PC1 agrees well (r = 0.89) with the KOE T400 time series (Figure 10b). Our KOE region (square in Figure 10) locates near the center of action of EOF1,

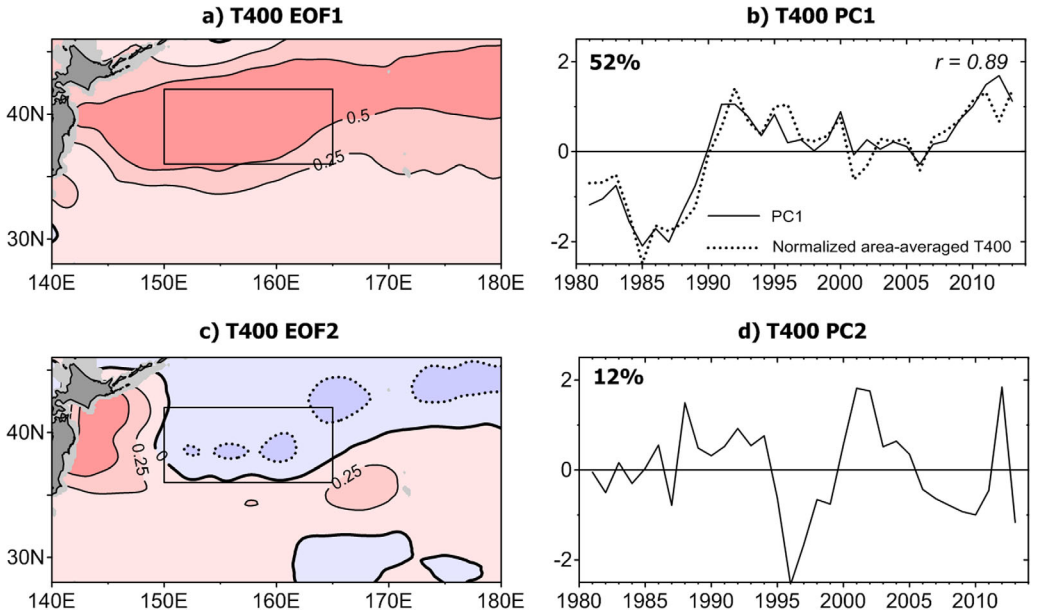

Figure 10. (a, c) EOFs and (b, d) corresponding PC time series for two leading modes of winter T400 in the western North Pacific. The PCs are normalized, so that EOFs denote the spatial pattern when the PC is unity. Normalized area-averaged KOE T400 is shown with dotted line in (b).

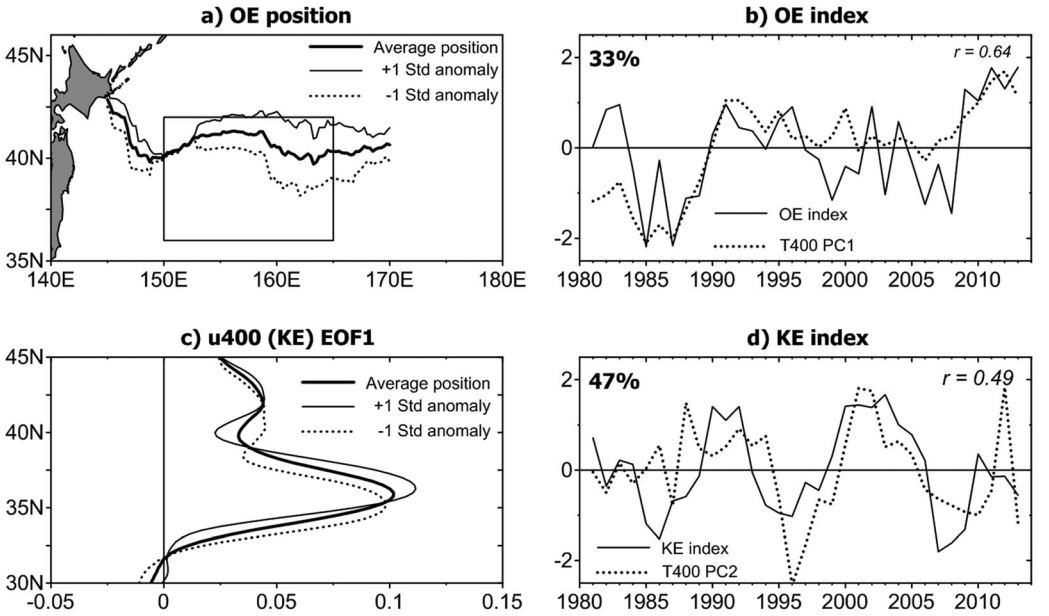

Figure 11. First EOFs (left panels) and corresponding PC time series (right) of (a−b) the latitudes of maximum meridional SST gradient representing the OE and (c−d) the zonal mean (145°−170°E) zonal velocity averaged from the surface to the 400 m (u400) representing the KE. The mean position of OE is shown with a thick solid line in Figure 11a together with their ±1 standard deviations with thin solid and dotted lines. The T400 PC1 from Figure 10b (solid line) is overlaid in Figure 11b. The mean position of KE is shown with thick solid line in Figure 11c together with their ±1 standard deviations with thin solid and dotted lines. The T400 PC2 from Figure 10d (solid line) is overlaid in Figure 11d.

indicating that the KOE region corresponds to the primary center of the upper-ocean thermal variability. The EOF2, which explains 12% of the total variance, shows a dipole pattern, with opposite signs especially between the KOE region and the Kuroshio recirculation south of the KE front (Figure 10c).

We investigate here the meridional shifts of the OE and KE in association with the T400 variability in Figure 10, since it has been suggested that the OE and KE variations have an important role in the interannual to decadal SST variability in the KOE region [*Taguchi et al*., 2007; *Nonaka et al*., 2008]. The OE index is defined following *Frankignoul et al*. [2011] as the PC1 of the latitudes of maximum meridional gradient of winter SST for the longitudes between 145°E and 170°E. The EOF1 explains 33% of the total variance and shows a meridional shift up to 2° in latitude especially to the east of 152°E (Figure 11a). The overall position of our model-derived OE front (thick line) matches well the observations-derived OE front of *Frankignoul et al*. [2011]. Our OE index is well correlated ($r = 0.64$) with the PC1 of T400 (Figure 11b), which is also true with the area averaged T400 in the KOE region ($r = 0.62$), suggesting that the KOE region thermal variability (and EOF1 of T400 over the western North Pacific) is primarily associated with the meridional shift of the OE front. This significant positive correlation between the OE index and KOE T400 means that warm (cold) anomalies tend to appear when the OE shifts northward (southward), in agreement with *Frankignoul et al*. [2011].

To investigate the influence of the KE on the KOE thermal variability, we have also performed an EOF analysis on the zonal-mean zonal velocity averaged from the surface to the 400 m (u400 hereafter) over the entire latitudes of the study area, following a similar approach as *Taguchi et al*. [2007]. The EOF1 of u400 (Figure 11c) explains 47% of the total variance and the average position of the maximum u400 is located at 36°N, with a plus and minus one standard deviation locating at about 1° north and south of the mean latitude. As the EOF1 of u400 represents the meridional shift of the KE, the corresponding PC1 (Figure 11d) is defined as the KE index. Our KE index is insignificantly correlated ($r = 0.35$) with the T400 PC1, but it is relatively well correlated ($r = 0.49$) with the T400 PC2 (Figure 11d), suggesting that the second mode temperature variability in the western North Pacific is associated with the meridional shift of KE. Since the KOE T400 is mainly related with T400 PC1 and little related with T400 PC2, the meridional shift of KE poorly explains the KOE T400 variability.

Table 1. Lag Correlations Between the Decadal Variability of Meridional Shift of Oceanic Fronts (OE and KE) and Lagged Atmospheric Circulation Patterns (WP and PNA)[a]

	OE Index		KE Index	
Lag	WP	PNA	WP	PNA
0	**−0.41**	−0.20	−0.14	0.12
M1 (NDJ)	−0.20	−0.35	−0.13	0.22
M2 (OND)	−0.00	**−0.42**	−0.03	0.15
1	−0.18	−0.30	0.10	−0.13
2	−0.03	**−0.37**	0.30	−0.08
3	**0.51**	−0.12	0.23	0.06
4	**0.38**	−0.20	0.12	0.11

[a]The nonzero lag without "M" indicates the number of years lead by the atmospheric forcing. The lags M1 and M2 indicate when the atmospheric indices lead DJF oceanic indices by 1 and 2 months, NDJ and OND, respectively. Significant correlations at the 95% confidence level are marked in boldface.

In addition to the meridional shift, our KE index is also associated with a strength change in u400, with a northward (southward) shift corresponding to a strengthening (weakening) of the KE jet. This is consistent with results of *Qiu and Chen* [2005] based on observational data, but differs from *Taguchi et al*. [2007] who claimed, based on results from an eddy-resolving OGCM similar to ours, the existence of two independent EOF modes of the KE variability: a meridional mode versus a strength mode.

The WP and PNA are the two major winter atmospheric circulation patterns in the North Pacific [*Wallace and Gutzler*, 1981]. The sea level pressure expressions of these midtropospheric stationary circulation patterns are the NPO and North Pacific (or Aleutian low) pattern, respectively [*Wallace and Gutzler*, 1981]. According to *Pak et al*. [2014], the PNA and Aleutian low intensity are well correlated to each other ($r = 0.92$) regardless of epochs, and so as in the relationship between WP and NPO ($r = 0.80$).

The linkage between atmospheric circulation patterns and wind stress curl in the North Pacific has been documented. *Ishi and Hanawa* [2005] showed that the correlation maps of wind stress curl in the North Pacific with PNA and Aleutian low intensity indices are similar and resemble the spatial pattern of the 1st mode variability of wind stress curl. They also showed the linkage between the 2nd mode of wind stress curl and WP. The regression map of wind stress curl anomaly to PC2 of SLP in the North Pacific [*Ceballos et al*., 2009], one of the definitions of the NPO index [*Linkin and Nigam*, 2008], shows a dipole pattern similar to the spatial pattern of the second mode variability of wind stress curl. These studies suggest that the major atmospheric circulation patterns, WP and PNA, represent the surface wind stress curl forcing in the North Pacific.

The OE index is significantly correlated with both the WP and PNA indices but with different lags between zero and 4 years (Table 1). At zero lag, it is significantly correlated with the WP ($r = -0.41$) but not with the PNA ($r = -0.20$). Significant correlation between PNA and OE index is found when PNA leads OE by 2 months (M2 in Table 1). This is consistent with the results of *Nonaka et al*. [2008] and *Frankignoul et al*. [2011], who attributed the meridional shift of the OE to the rapid barotropic response to the Aleutian low mode, surface expression of the PNA. In addition to the significant correlation with the WP at zero lag and PNA at two months lag, the OE index reveals a significant lagged response to both the WP ($r = 0.51$ at lag 3 yr and $r = 0.38$ at lag 4 yr) and PNA ($r = -0.37$ at lag 2 yr), which can be explained by the slow response to wind stress curl anomalies and baroclinic Rossby wave adjustment [*Nonaka et al*., 2008; *Frankignoul et al*., 2011]. On the other hand, the KE index has no significant correlations with both the WP and PNA indices at any lag (Table 1). Although insignificant at the 95% confidence level, the highest correlation ($r = 0.30$ at lag 2 yr) occurs between the KE and WP indices.

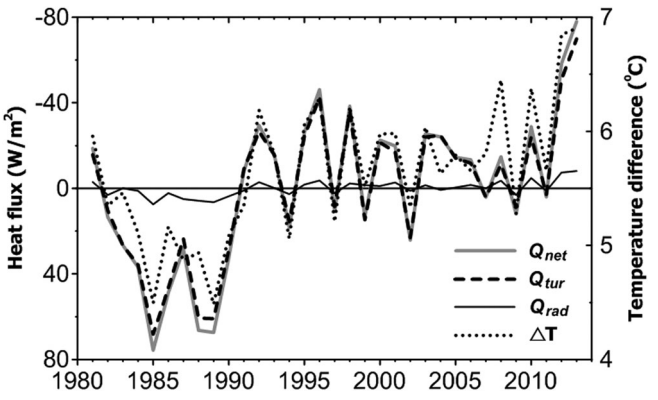

Figure 12. Annual time series of area-mean winter (DJF) air-sea temperature difference (ΔT, dotted line) and surface heat flux components over the KOE region. The net surface heat flux (Q_{net}), turbulent heat fluxes (Q_{tur}), and radiative heat fluxes (Q_{rad}) are shown with thick solid, dashed, and thin solid lines, respectively.

4.2. Relationship Between Winter Q_{net} and KOE Temperature: Ocean-to-Atmosphere Feedback

The previous subsection showed the ocean dynamics, represented by ADV in our study, is important in determining

the upper-ocean thermal variability (also SST variability) in the KOE region. Since the SST forcing on the overlying atmosphere exerted by strong ocean dynamics is known to be prevalent in the KOE region, SST is expected to be a dominant factor in causing the Q_{net} variability in the KOE region. The interannual to decadal variability of Q_{net} in the KOE region is mainly due to the surface turbulent heat fluxes (Q_{tur}) with a negligible contribution from the net radiative fluxes (Figure 12).

Following *Tomita et al*. [2002], the linearized anomalous latent (Q'_{lat}) and sensible (Q'_{sen}) turbulent heat fluxes can be written in terms of wind speed (W), SST (T_s), surface air temperature (T_a), and humidity at the sea surface (q_s) and at 10 m aloft (q_a), such as:

$$Q'_{lat} = \rho_a L C_L \left\{ q'_s \overline{W} - q'_a \overline{W} + W' (\overline{q_s} - \overline{q_a}) \right\} = \rho_a L C_L \left(\Delta q' \overline{W} + W' \overline{\Delta q} \right), \quad (5)$$

$$Q'_{sen} = \rho_a c_p C_S \left\{ T'_s \overline{W} - T'_a \overline{W} + W' \left(\overline{T_s} - \overline{T_a} \right) \right\} = \rho_a c_p C_S \left(\Delta T' \overline{W} + W' \overline{\Delta T} \right), \quad (6)$$

where ρ_a is the air density, c_p is the specific heat of air at constant pressure, L is the latent heat of vaporization of water, and C_L and C_S are bulk transfer coefficients for latent heat and sensible heat, respectively; overbars and primes indicate the climatological mean and anomalies, respectively, and $\Delta q' \equiv q'_s - q'_a$, $\overline{\Delta q} \equiv \overline{q_s} - \overline{q_a}$, $\Delta T' \equiv T'_s - T'_a$, $\overline{\Delta T} \equiv \overline{T_s} - \overline{T_a}$.

Calculation of nonlinear terms such as $\Delta q' W'$ and $\Delta T' W'$ using model SST and ERA interim indicates their negligible contribution to sensible and latent heat fluxes. Therefore, we examine here only the linear influences of ΔT, Δq, and W, which explain most of Q'_{lat} and Q'_{sen}. In order to compare the relative importance among different parameters having different measuring units, we have regressed the turbulent heat flux terms on each normalized parameters (Table 2). Table 2 therefore shows the change in turbulent heat flux in W m^{-2} per one standard deviation change of each parameter.

Table 2 clearly shows that the ocean-atmosphere temperature difference (ΔT = SST - T_a) is the most important predictor for nonseasonal variations of Q_{tur} and therefore Q_{net} (Figure 12). Although the bulk formula for the latent heat flux does not explicitly contain ΔT, ΔT is most strongly correlated with Q_{tur} due to SST influence on specific humidity at the sea surface. Indeed, ΔT and Δq are very well correlated to each other ($r = 0.81$). Δq and W, which form two key parameters for determining the latent heat flux, are also important, but with smaller regression coefficients compared to that of ΔT in the Q_{tur} and Q_{net} regressions (Table 2). Indeed, the correlation coefficient of nonseasonal winter Q_{tur} with ΔT is -0.87 for the entire period, while those with Δq and W are -0.77 and -0.49, respectively. This predominant relationship between ΔT and Q_{tur} is also observed for both E1 ($r = -0.78$) and E2 ($r = -0.81$) periods.

Positive Q_{net} anomalies are observed during E1 (a strong EAWM period) in the KOE region (Table 3), indicating lesser oceanic heat loss to the atmosphere compared to that during E2 (a weak EAWM period). Also, the mean wind speed is slightly higher during E2 (Table 3), consistent with *Park et al*. [2012] who showed the recent strengthening tendency of wind speed in the KOE region after 1990 [*Park et al*., 2012, Figure 5b]. Indeed, the wind speed increased during E2 for the most region of our domain including the KOE region (Figure 13b), indicating a minor influence of the EAWM. Consistent with these results, the SST variations in our KOE region are only moderately influenced by the monsoon even during the strong monsoon period (1970 − 1989) according to *Park et al*. [2012, Figure 6]. Moreover, Table 2 suggests that the Q_{tur} variability in the KOE region is preferentially determined by ΔT, rather than by wind speed, for which the abrupt SST rise

Table 2. Regression Coefficients Between Winter Heat Flux Components and Winter Meteorological Variables[a]

	T_a	SST	ΔT	q_a	q_s	Δq	W
Latent (20.23)	−2.97	**−15.05**	**−17.86**	−2.39	**−14.85**	**−17.91**	**−8.56**
Sensible (13.01)	2.26	**−6.87**	**−12.17**	2.33	**−6.65**	**−10.10**	**−5.56**
Q_{tur} (32.74)	−0.71	**−21.92**	**−30.03**	−0.06	**−21.50**	**−28.02**	**−14.12**
Q_{net} (36.00)	−0.12	**−23.95**	**−33.54**	0.70	**−23.48**	**−31.07**	**−14.58**

[a] Q_{tur}: turbulent heat fluxes, Q_{net}: net heat flux, T_a: air temperature, SST: sea surface temperature (or mixed layer temperature), ΔT: SST minus T_a, q_a: specific humidity of atmosphere, q_s: specific humidity of sea surface, Δq: q_s minus q_a, W: wind speed. The regression coefficients having a significant correlation at the 95% confidence level are marked in boldface. The standard deviation of each heat flux component is given (in W m^{-2}) in parentheses. The sign convention is such that if the sign is minus, for example, the upward turbulent fluxes increase when ΔT increases.

Table 3. Epoch Means of Winter (DJF) Variables Averaged Over the KOE Region (150°–165°E, 36°–42°N) and the SRG Region (145°–160°E, 30°–34°N) Obtained From Spatially Nonfiltered Data[a]

Region	Period	W ($m\ s^{-1}$)	T_a (°C)	SST (°C)	ΔT (°C)	Q_{tur} ($W\ m^{-2}$)
KOE	1981–1990 (E1)	−0.16	−0.35	−0.90	−0.55	+35.58
	1991–2008 (E2)	+0.11	+0.11	+0.26	+0.15	−11.82
	1981–2013 (All)	10.71	7.46	13.10	5.65	−326.19
SRG	1981–1990 (E1)	−0.11	−0.21	−0.16	+0.05	+2.42
	1991–2008 (E2)	+0.10	+0.09	+0.04	−0.05	−1.98
	1981–2013 (All)	9.51	15.54	19.25	3.71	−276.48

[a]Note that the values for subperiods (E1 and E2) are anomalies relative to the mean value over the total period (All), while the values for the total period include epoch-mean values.

as much as 1.16°C from E1 to E2, compared to a modest increase of 0.46°C in T_a (Table 3), plays a decisive role in producing a spectacular difference in heat loss to the atmosphere (47.4 W m^{-2}) (see Table 3) between the two periods. In addition, an increase in the wind speed by 0.27 m s^{-1} also contributes to the increase in oceanic heat loss during E2. Figures 13a and 13c show that the epoch change of Q_{tur} is mostly determined by the change in ΔT except for the southern recirculation gyre (SRG, 145°−160°E, 30°−34°N) where both Q_{tur} and ΔT are decreased after 1990, suggestive of the stronger influence of the wind speed change. The increased oceanic heat loss during E2 in the SRG region as compared to that during E1 can only be explained by an increase in wind speed (by +0.21 m s^{-1}), because ΔT is decreased by −0.10°C thus contributing to a positive trend of Q_{tur}. It is also interesting to remark that both T_a and SST are increased during E2 compared to E1 regardless of the region, however, the comparatively larger increase in SST (T_a) has resulted in the increase (decrease) of ΔT in the KOE (SRG) region (see Table 3). This attests that the interannual to decadal variability of winter Q_{net} in the KOE region after the 1990 regime shift (E2) is governed mostly by ocean dynamics (SST change), while that in the SRG by the atmosphere (wind speed change).

The nature of the ocean-atmosphere interactions can also be diagnosed using the local correlation between Q_{net} and SST [*Wu et al*., 2006; *Wu and Kirtman*, 2007; *Wu and Kinter*, 2010; *Park et al*., 2012]. We find a systematic negative correlation between Q_{net} and SST or T400 for cool seasons from November to May (Figure 14). The strongest negative correlation occurs when both SST and T400 lead Q_{net} by a few months centered at 2 months, indicating a negative feedback of the ocean-atmosphere interactions. Positive (negative) ocean temperature anomalies induce upward (downward) turbulent heat flux anomalies due to an increase (decrease) in temperature difference between the sea surface and overlying atmosphere, which in turn results in a negative (positive) temperature tendency according to (3), acting to dampen the upper-ocean temperature increase. Our results are consistent with the coupled climate model results of *Kwon and Deser* [2007]. It is worth stressing that the maximum correlation coefficients of Q_{net} with T400 ($r = -0.81$ for NDJ T400 and FMA Q_{net}) is higher than those with SST ($r = -0.72$ for DJF SST and FMA Q_{net}), supporting that the upper-ocean heat content is a better predictor than SST for the ocean-atmosphere heat exchange [*Deser et al*., 2003; *Dawe and Thompson*, 2007; *Kelly et al*., 2010]. Due to the long autocorrelation time scale of T400, the area of significant correlation between Q_{net} and T400 is elongated along the y-axis in Figure 14a.

4.3. Causes of Increased Contribution of Q_{net} During E1

We showed in section 3.3 the epoch-dependent contributions of Q_{net} and ADV to winter HSR in the KOE region. Q_{net} has stronger temporal variability compared to ADV during E1, while ADV dominates during E2. Here, we explore the causes of the change of contribution of each Q_{net} and ADV for two contrasting periods. As shown in section 3.3, the standard deviation of Q_{net} has significantly decreased during E2 (48.0 W m^{-2} during E1 and 19.4 W m^{-2} during E2, Table 4), while the standard deviation of ADV is not much sensitive to the different epochs (27.7 W m^{-2} during E1 and 27.4 W m^{-2} during E2, Table 4). This significant (insignificant) difference of standard deviation of Q_{net} (ADV) during E1 and E2 periods suggests that the epoch-dependent change of the relative contribution of Q_{net} and ADV to HSR arise from the decadal change of temporal variability of Q_{net}.

We have above mentioned that the variability of Q_{net} is mostly determined by the ΔT in the KOE region (Tables 2 and 3). Indeed, the standard deviation of ΔT in the KOE region are also significantly different showing 0.70°C and 0.41°C during E1 and E2 periods, respectively (Table 4). The standard deviation of SST during both periods also shows significant difference, while the difference of standard deviation for two

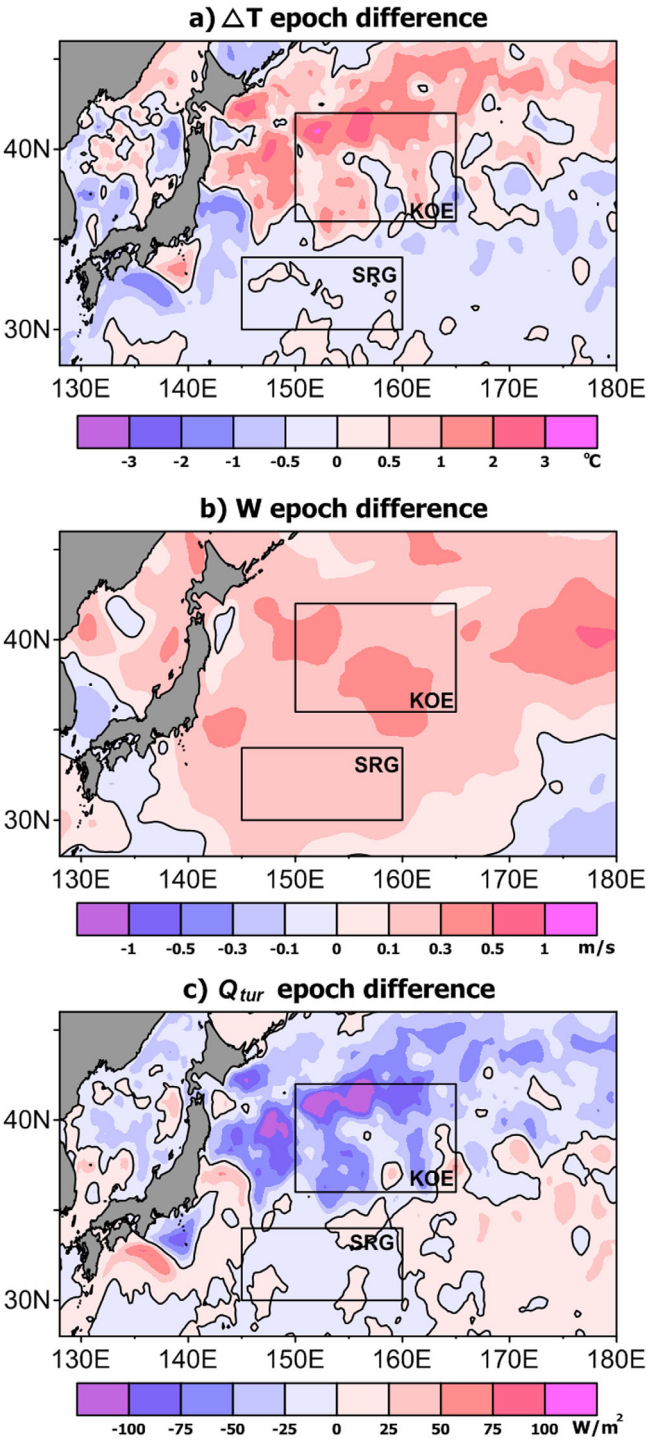

Figure 13. Spatial distribution of the epoch difference (1991–2008 minus 1981–1990) of (a) air-sea temperature difference (ΔT, SST – Ta in °C), (b) wind speed (W in m s^{-1}), and (c) turbulent heat flux (Q_{tur} in W m^{-2}) obtained from 0.25°×0.25° gridded values.

periods is insignificant for T_a (Table 4), suggesting that the SST variability or the upper-ocean thermal variability is important for the decadal change of ΔT, that is Q_{net}, variability.

The depth-averaged temperature (T400) can be reconstructed and the contribution of each heat budget term (HSR, Q_{net}, ADV) to the winter temperature variability in the KOE region can be quantified using the temperature tendency equation (3). We integrate (3) temporally from the January of the previous year to the January of the present year to represent the T400 of January of the present year, the center month of our winter definition (December-February). More precisely, the winter T400 associated with each heat budget term can be reconstructed as:

$$T400_r(yr) = T400_r(yr-1) + \Delta t \times \left\langle \frac{\partial T}{\partial t} \right\rangle_{yr-1}, \quad (7)$$

where $T400_r$ is the reconstructed T400 during winter and yr indicates the calendar year. Δt denotes the integration time scale, 1 year. The tendency term $\frac{\partial T}{\partial t}$ includes Q_{net} and ADV divided by $\rho c_p h$, the sum of which is HSR (See (3)). The bracket ($\langle\ \rangle_{yr}$) denotes the annual average of yr from January to the following January. Integrating January to January temperature tendency term, we can reconstruct KOE T400 series of January, the center month of our winter (DJF). The corresponding annual time series of reconstructed winter temperature are denoted by $T400_r^Q$, $T400_r^{ADV}$, and $T400_r^{HSR}$, respectively (Figure 15). Because of negligible residuals RES, ADV is computed as the difference between HSR and Q_{net}. $T400_r^Q$ and $T400_r^{ADV}$ have opposing linear trends reaching up to almost 3°C yr^{-1} in the KOE region (not shown), thus mostly compensating each other to yield a small net warming trend of about 0.06°C yr^{-1}. Because we are using nonseasonal anomalies of each heat budget term, the record-length average of each heat budget term is not considered in (7). Therefore, the reconstructed T400 due to each heat budget term should be zero at the end of reconstruction (January 2013) because we assumed T400 is zero at the start (January 1981). The correlation between KOE T400 and KOE $T400_r^{HSR}$ is higher than 0.9, implying that the reconstructed T400 well represents the KOE T400.

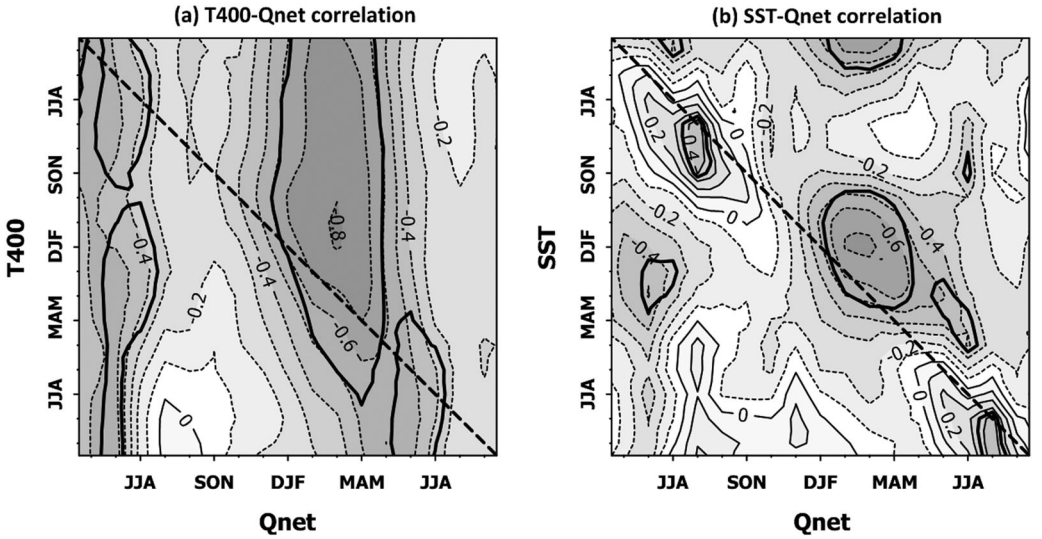

Figure 14. Lagged correlation of (a) T400 and (b) SST with Q_{net} for different months during 1981 − 2013 in the KOE region. JJA, SON, DJF, and MAM denote the averaging months used for constructing yearly time series: for example, DJF means December through February, etc. Negative correlation coefficients are marked with dotted line. The significant correlations at 95% confidence level are marked with thick lines.

As expected from the time series of annual-averaged Q_{net} shown in Figure 8a, $T400_r^Q$ increases during E1, while it decreases afterward. $T400_r^{ADV}$ varies in opposition to $T400_r^Q$ with a high negative correlation of −0.94 when $T400_r^{ADV}$ leads by 2 yr. These out of phase variations further strengthen the negative feedback paradigm of ocean-atmosphere interactions in the KOE region, in which Q_{net} is mainly controlled by ocean advection-induced T400 anomalies. In short, the KOE T400 anomaly is determined by ADV and 2 yr lagged response of Q_{net} to ADV variability, regardless of period. However, as described in Table 4, the SST variability (much related to T400 variability) is significantly higher, so that Q_{net} variability is much higher during E1 period compared to those during E2 period. This means that ocean dynamics (ADV) plays a primary role in determining the upper-ocean thermal variability in the KOE region, which makes stronger and weaker temporal variability of Q_{net} during E1 and E2 periods, respectively. However, it is not obvious how the combined effects of ADV and lagged Q_{net} response to ADV cause the different degree of SST variability in the KOE region during E1 and E2 periods shown in Table 4, which needs to be further investigated in future. Because temporal variability of ADV is not much sensitive to the epochs (Table 4), Q_{net} could play important role to the HSR variability due to its stronger variability during E1 period.

5. Summary and Concluding Remarks

Based on the MERCATOR 1/12°-resolution OGCM ORCA12, we have investigated the upper 400 m heat budget and the winter temperature variability in the KOE region where the ocean-atmosphere interaction is strongest in the North Pacific. Validation against observational data indicates that the model reproduces realistically the KOE region thermal variability with high correlations. In addition, the model heat budget is well closed in that HSR (heat storage rate) is nearly perfectly balanced with the sum of Q_{net} (net surface heat flux) and ADV (ocean heat advection), with a negligible residual. As in previous heat budget studies in the KOE region [*Vivier et al.*, 2002; *Kwon and Deser*, 2007], the seasonal variability of HSR is primarily explained by Q_{net} and secondarily by ADV, while its interannual variability is dominated by ADV during the entire period (1981 − 2013). A new finding of our study is that there is a significant

Table 4. Standard Deviations of Winter (DJF) Variables Averaged Over the KOE Region (150°−165°E, 36°−42°N)[a]

Variables	E1 (1981–1990)	E2 (1991–2008)	F-test
Q_{net} (W m^{-2})	48.0	19.4	O
ADV (W m^{-2})	27.7	27.4	X
ΔT (°C)	0.70	0.41	O
SST (°C)	1.16	0.53	O
T_a (°C)	0.66	0.55	X

[a]F-test column is filled with "O" if the standard deviation of two periods is significantly different at 95% confidence level.

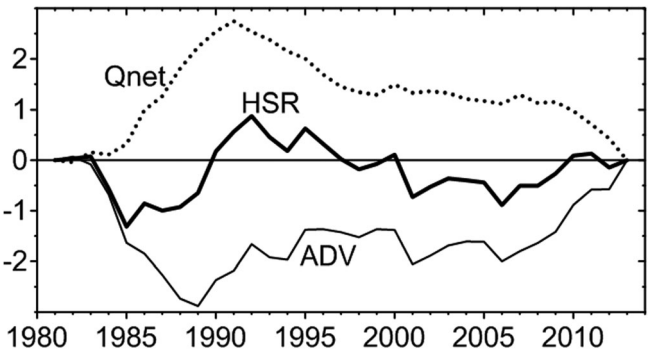

Figure 15. Area averaged reconstructed T400 time series obtained from annual averaged HSR ($T400_r^{HSR}$, thick line), Q_{net} ($T400_r^{Q}$, dotted line), and ADV ($T400_r^{ADV}$, thin line) in the KOE region with a unit of °C.

epoch-dependent change in the relative contribution of Q_{net} and ADV to winter HSR for two periods before and after the 1990 regime shift. During the E1 period (1981 − 1990), the temporal variability (standard deviation) of Q_{net} (48.0 W m^{-2}) is stronger than that of ADV (27.7 W m^{-2}) in the KOE region. While they become 19.4 W m^{-2} and 27.4 W m^{-2}, respectively, during the E2 period (1991 − 2008), suggesting that Q_{net} (ADV) plays important role for the HSR variability in the KOE region during E1 (E2) period. These model-derived results nicely confirm the observational evidence highlighted in *Park et al*. [2012], who showed in the western North Pacific a strong atmospheric influence on the SST variability during the strong EAWM period before 1990 [see also *Pak et al*., 2014] but increasingly important ocean dynamics especially in the KOE region during the weak EAWM period after 1990. However, in the present study the upper-ocean thermal variability in the KOE region is not directly influenced by the EAWM, which deserves further research in future work.

The comparison between the two leading PC time series of T400 and the OE and KE indices suggests that the interannual to decadal upper-ocean thermal variability in the western North Pacific is controlled primarily by the meridional shift of the OE front and secondarily by that of the KE front. The OE index explains also well the area-averaged KOE T400 as well as the EOF1 of T400 in the western North Pacific. The meridional shift of the OE is significantly correlated with both the WP and PNA patterns at multiple lags between 0 and 4 yr, suggesting the meridional shift of OE is influenced by both barotropic and baroclinic Rossby wave dynamics triggered by atmospheric forcing, consistent with previous studies [*Nonaka et al*., 2008; *Frankignoul et al*., 2011]. The EOF2 of T400 is well explained by the KE index, showing the northward (southward) shift concomitant with the strengthening (weakening) of the KE front, in agreement with *Qiu and Chen* [2005], but in contrast to *Taguchi et al*. [2007] who claimed the existence of two independent modes of the meridional displacement and strength of the KE.

In the KOE region, the turbulent heat flux (Q_{tur}), which dominates the Q_{net} variability, is best explained by the sea-air temperature difference (ΔT) rather than wind speed or humidity difference, suggesting that the Q_{net} variability of the region is not directly controlled by the atmosphere. The E1 period is characterized by the positive Q_{net} anomaly (less heat loss from the ocean), and smaller ΔT and wind speed as compared to those during the E2 period, in complete opposition to the expected negative Q_{net} anomaly (larger heat loss from the ocean) and stronger wind if the Q_{net} variability would be under direct control of the winter monsoon. This indicates that the temperature difference between ocean and atmosphere, mainly caused by changes in SST, is a critical factor in determining the Q_{net} variability in the KOE region, thus the ocean-to-atmosphere feedback or the negative Q_{net} feedback. The strong negative correlation between the winter ocean temperature and lagged Q_{net} (Table 3) further evidences the negative Q_{net} feedback damping the temperature anomaly driven by the ocean dynamics (ADV).

In line with the above result, the decadal changes of contribution of Q_{net} and ADV to the KOE HSR during two contrasting epochs are explained by the difference in the standard deviation of SST during each of the two epochs, which in turn results in the variability of Q_{net} in those two epochs. During E1 period, temporal variability of SST, that is ΔT, in the KOE region is significantly higher than that during E2. This thermal variability is partly ($r = 0.6$) due to the ocean dynamics represented by meridional shift of OE. The 2 yr-lagged response of reconstructed T400 due to Q_{net} to that due to ADV suggest that ocean dynamics plays an important role for determining upper-ocean thermal variability in the KOE region, which yields stronger and weaker temporal variability of Q_{net} during E1 and E2 periods, respectively. Because the ADV variability in each epoch is not much different, the epoch-dependent Q_{net} variability plays a relatively important role to the HSR variability during E1 period compared to E2 period. It should be noted that, although the temporal standard deviation of ADV is not much sensitive to the different epochs (Table 4), the epoch-mean of the

anomaly of KOE ADV is somewhat different (Figure 8a). Because ocean temperature anomaly induced by ADV variability is shown to cause Q_{net} variability, it will be also interesting to investigate the reason for the difference of mean KOE ADV during E1 and E2 periods, which has not been addressed in this study. In short, it is imperative to investigate the long-term variability of ADV for understanding the KOE T400 variability.

Our model-derived results, which show the predominant role of ocean advection for the KOE thermal variability especially after the 1990 regime shift, are well consistent with previous work [*Park et al*., 2012]. To our knowledge, this is the first to report that a high resolution OGCM like ORCA12 is sufficiently realistic enough to complement the observations in a data-poor area for investigating the decadal-scale upper-ocean variability. While the previous study has only qualitatively inferred via statistical methods, we have shown quantitatively the different main contributor of heat storage rate in the KOE region before and after 1990 regime shift resorting to the model results.

Acknowledgments
We thank the anonymous reviewers for their many insightful comments and suggestions. We also thank to members of Mercator Ocean for their efforts in the model developments. The ORCA12 has been integrated at Météo-France on a BULL computer. ORCA12 may be obtained from RB (romain.bourdalle-badie@mercator-ocean.fr). The Base10 topography was developed at the LEGOS Laboratory (Toulouse, France) by F. Lyard (lyard@legos.obs-mip.fr). This work was supported by EAST-I project, funded by Ministry of Oceans and Fisheries, Korea.

References

Adcroft, A., C. Hill, and J. Marshall (1997), Representation of topography by shaved cells in a height coordinate ocean model, *Mon. Weather Rev.*, *125*, 2293–2315.

Alexander, M. A., J. D. Scott, and C. Deser (2000), Processes that influence sea surface temperature and ocean mixed layer depth variability in a coupled model, *J. Geophys. Res.*, *105*, 16,823–16,842, doi:10.1029/2000JC900074.

Amante, C., and B. W. Eakins (2009), ETOPO1 1 Arc-Minute Global Relief Model: Procedures, data sources and analysis, *NOAA Tech. Memo. NESDIS NGDC-24*, 19 pp., National Geophysical Data Center, NOAA, Colo.

An, S.-I (2008), A mechanism for the multi-decadal climate oscillation in the North Pacific, *Theor. Appl. Climatol.*, *91*, 77–84.

Arakawa, A., and V. R. Lamb (1981), A potential enstrophy and energy conserving scheme for the shallow water equations, *Mon. Weather Rev.*, *109*, 18–36.

Barnier, B., et al. (2006), Impact of partial steps and momentum advection schemes in a global circulation model at eddy permitting resolution, *Ocean Dyn.*, *56*(5-6), 543–567, doi:10.1007/s10236-006-0082-1.

Becker, J. J., et al. (2009), Global bathymetry and elevation data at 30 arc seconds resolution: SRTM30_PLUS, *Mar. Geod.*, *32*(4), 355 – 371.

Bond, N. A., J. E. Overland, M. Spillane, and P. Stabeno (2003), Recent shifts in the state of the North Pacific, *Geophys. Res. Lett.*, *30*(23), 2183, doi:10.1029/2003GL018597.

Boris, J. P., and D. L. Book (1973). Flux-corrected transport, I: SHASTA, a fluid transport algorithm that works, *J. Comput. Phys.*, *11*, 38–69.

Bouillon, S., M. A. M. Maqueda, V. Legat, and T. Fichefet (2009), An elastic-viscous-plastic sea ice model formulated on Arakawa B and C grids, *Ocean Modell.*, *27*, 174–184.

Cayan, D. R. (1992), Latent and sensible heat flux anomalies over the Northern Oceans: Driving the sea surface temperature, *J. Phys. Oceanogr.*, *22*, 859–881.

Ceballos, L. I., E. Di Lorenzo, C. D. Hoyos, N. Schneider, B. Taguchi (2009), North Pacific Gyre Oscillation synchronizes climate fluctuations in the eastern and western boundary systems, *J. Clim.*, *22*, 5163–5174.

Cheng, Y.-H., C.-R. Ho, Q. Zheng, and N.-J. Kuo (2014), Statistical characteristics of mesoscale eddies in the North Pacific derived from satellite altimetry, *Remote Sens.*, *6*, 5164–5183.

Dai, A., and K. E. Trenberth (2002), Estimates of freshwater discharge from continents: Latitudinal and seasonal variations, *J. Hydrometeorol.*, *3*, 660–687.

Dawe, J. T., and L.A. Thompson (2007), PDO-related heat and temperature budget changes in a model of the North Pacific, *J. Clim.*, *20*, 2092–2108.

Dee, D. P., et al. (2011), The ERA-Interim reanalysis: Configuration and performance of the data assimilation system, *Q. J. R. Meteorol. Soc.*, *137*, 553–597.

Deser, C., M. A. Alexander, and M. S. Timlin (1999), Evidence for a wind-driven intensification of the Kuroshio current extension from the 1970s to the 1980s, *J. Clim.*, *12*, 1697–1706.

Deser, C., M. A. Alexander, and M. S. Timlin (2003), Understanding the persistence of sea surface temperature anomalies in mid-latitudes, *J. Clim.*, *16*, 57–72.

Di Lorenzo, E., et al. (2008), North Pacific gyre oscillation links ocean climate and ecosystem change, *Geophys. Res. Lett.*, *35*, L08607, doi:10.1029/2007GL032838.

Emery, W. J., and R. E. Thomson (1997), *Data Analysis Methods in Physical Oceanography*, 638 pp., Pergamon Press, New York.

Frankignoul, C., N. Sennechael, Y.-O. Kwon, and M. A. Alexander (2011), Influence of the meridional shifts of the Kuroshio and the Oyashio extensions on the atmospheric circulation, *J. Clim.*, *24*, 762–777.

Grodsky, S. A., J. A. Carton, H. Liu (2008), Comparison of bulk sea surface and mixed layer temperatures, *J. Geophys. Res.*, *113*, C10026, doi:10.1029/2008JC004871.

Hosoda, S., M. Nonaka, T. Tomita, B. Taguchi, H. Tomita, and N. Iwasaka (2015), Impact of downward heat penetration below the shallow seasonal thermocline on the sea surface temperature, *J. Oceanogr.*, *71*, 541–556.

Ishi, Y., and K. Hanawa (2005), Large-scale variabilities of wintertime wind stress curl field in the North Pacific and their relation to atmospheric teleconnection patterns, *Geophys. Res. Lett.*, *32*, L10607, doi:10.1029/2004GL022330.

Jo, H.-S., S.-W. Yeh, and C.-H. Kim (2013), A possible mechanism for the North Pacific regime shift in winter of 1998/1999, *Geophys. Res. Lett.*, *40*, 4380–4385, doi:10.1002/grl.50798.

Kalnay, E., et al. (1996), The NCEP/NCAR 40-year reanalysis project, *Bull. Am. Meteorol. Soc.*, *77*, 437–471.

Kelly, K. A., and S. Dong (2004), The relationship of western boundary current heat transport and storage to mid-latitude ocean-atmosphere interaction, in *Earth's Climate*, edited by C. Wang, S. P. Xie and J. A. Carton, AGU, Washington, D. C., doi:10.1029/147GM19.

Kelly, K. A., R. J. Small, R. M. Samelson, B. Qiu, T. M. Joyce, Y.-O. Kwon, and M. F. Cronin (2010), Western boundary currents and frontal air-sea interaction: Gulf stream and Kuroshio extension, *J. Clim.*, *23*, 5644–5667.

Kwon, Y.-O., and C. Deser (2007), North Pacific decadal variability in the Community Climate System Model version 2, *J. Clim.*, *20*, 2416–2433.

Kwon, Y.-O., M. A. Alexander, N. A. Bond, C. Farnkignoul, H. Nakamura, B. Qiu, and L. A. Thompson (2010), Role of the Gulf Stream and Kuroshio-Oyashio systems in large-scale atmosphere-ocean interaction: A review, *J. Clim.*, *23*, 3249–3281.
Large, W. G., and S. G. Yeager (2004), Diurnal to decadal global forcing for ocean and sea-ice models: The data sets and flux climatologies, *NCAR Tech. Rep. TN-460+STR*, 105 pp., National Center for Atmospheric Research, Colo.
Latif, M., and T. P. Barnett (1994), Causes of decadal climate variability over the North Pacific and North America, *Science*, *266*, 634–637.
Levitus, S., J. Antonov, T. Boyer (2005), Warming of the world ocean, 1995-2003, *Geophys. Res. Lett.*, *32*, L02604, doi:10.1029/2004GL021592.
Linkin, M. E., and S. Nigam (2008), The North Pacific Oscillation-west Pacific teleconnection pattern: Mature-phase structure and winter impacts, *J. Clim.*, *21*, 1979–1997.
Madec, G. (2008), NEMO ocean engine. Note du Pôle de Modélisation, *Inst. Pierre-Simon Laplace*, Paris.
Madec, G., and M. Imbard (1996), A global ocean mesh to overcome the North Pole singularity, *Clim. Dyn.*, *12*, 381–388.
Mantua, N. J., and S. R. Hare (2002), The Pacific Decadal Oscillation, *J. Oceanogr.*, *58*, 35–44.
Miller, A. J., F. Chai, S. Chiba, J. R. Moisan, and D. J. Neilson (2004), Decadal-scale climate ecosystem interactions in the North Pacific ocean, *J. Oceanogr.*, *60*, 163–188.
Moisan, J. R., and P. P. Niiler (1998), The seasonal heat budget of the North Pacific: Net heat flux and heat storage rates (1950-1990), *J. Phys. Oceanogr.*, *28*, 401–421.
Nakamura, H., G. Lin, and T. Yamagata (1997), Decadal climate variability in the North Pacific during the recent decades, *Bull. Am. Meteorol. Soc.*, *78*, 2215–2225.
Nonaka, M., and S.-P. Xie (2003), Covariations of sea surface temperature and wind over the Kuroshio and its extension: Evidence for ocean-to-atmosphere feedback, *J. Clim.*, *16*, 1404–1413.
Nonaka, M., H. Nakamura, Y. Tanimoto, T. Kagimoto, and H. Sasaki (2006), Decadal variability in the Kuroshio-Oyashio Extension simulated in an eddy-resolving OGCM, *J. Clim.*, *19*, 1970–1989.
Nonaka, M., H. Nakamura, Y. Tanimoto, and T. Kagimoto (2008), Interannual-to-decadal variability in the Oyashio and its influence on temperature in the subarctic frontal zone: An eddy-resolving OGCM simulation, *J. Clim.*, *21*, 6283–6303.
Pak, G., Y.-H. Park, F. Vivier, Y.-O. Kwon, and K.-I. Chang (2014), Regime-dependent nonstationary relationship between the East Asian winter monsoon and North Pacific oscillation, *J. Clim.*, *27*, 8185–8204.
Park, Y.-H., J.-H. Yoon, Y.-H. Youn, and F. Vivier (2012), Recent warming in the western North Pacific in relation to rapid changes in the atmospheric circulation of the Siberian high and Aleutian low systems, *J. Clim.*, *25*, 3476–3493.
Penduff, T., M. Juza, L. Brodeau, G.C. Smith, B. Barnier, J.-M. Molines, A.-M. Treguier, and G. Madec (2010), Impact of global ocean model resolution on sea-level variability with emphasis on interannual time scales, *Ocean Sci.*, *6*, 269–284.
Qiu, B. (2000), Interannual variability of the Kuroshio Extension system and its impact on the wintertime SST field, *J. Phys. Oceanogr.*, *30*, 1486–1502.
Qiu, B. (2001), Kuroshio and Oyashio currents, in *Encyclopedia of Ocean Sciences*, edited by J. H. Steele, pp. 1413–1425, Academic Press, New York, doi:10.1006/rwos.2001.0350.
Qiu, B. (2003), Kuroshio Extension variability and forcing of the Pacific Decadal Oscillations: Responses and potential feedback, *J. Phys. Oceanogr.*, *33*, 2465–2482.
Qiu, B., and S. Chen (2005), Variability of the Kuroshio Extension jet, recirculation gyre, and mesoscale eddies on decadal time scales, *J. Phys. Oceanogr.*, *35*, 2090–2103.
Qiu, B., and K. A. Kelly (1993), Upper-ocean heat balance in the Kuroshio Extension region, *J. Phys. Oceanogr.*, *23*, 2027–2041.
Qiu, B., N. Schneider, and S. Chen (2007), Coupled decadal variability in the North Pacific: An observationally constrained idealized model, *J. Clim.*, *20*, 3602–3620.
Reynolds, R. W., N. A. Rayner, T. M. Smith, D. C. Stokes, and W. Wang (2002), An improved in situ and satellite SST analysis for climate, *J. Clim.*, *15*, 1609–1625.
Sainz-Trapaga, S., and T. Sugimoto (2000), Three-dimensional velocity field and cross-frontal water exchange in the Kuroshio Extension, *J. Oceanogr.*, *56*, 79–92.
Schneider, N., and A. J. Miller (2001), Predicting western North Pacific Ocean climate, *J. Clim.*, *14*, 3997–4002.
Schneider, N., A. J. Miller, and D. W. Pierce (2002), Anatomy of North Pacific decadal variability, *J. Clim.*, *15*, 586–605.
Seager, R., Y. Kushnir, N. H. Naik, M. A. Cane, and J. Miller (2001), Wind-driven shifts in the latitude of the Kuroshio-Oyashio Extension and generation of SST anomalies on decadal timescales, *J. Clim.*, *14*, 4249–4265.
Seo, H., Y.-O. Kwon, and J.-J. Park (2014), On the effect of the East/Japan Sea SST variability on the North Pacific atmospheric circulation in a regional climate model, *J. Geophys. Res. Atmos.*, *119*, 418–444, doi:10.1002/2013JD020523.
Sugimoto, S., and K. Hanawa (2009), Decadal and interdecadal variations of the Aleutian low activity and their relation to upper oceanic variations over the North Pacific, *J. Meteorol. Soc. Jpn.*, *87*, 601–614.
Sugimoto, S., and K. Hanawa (2011), Roles of SST anomalies on the wintertime turbulent heat fluxes in the Kuroshio-Oyashio confluence region: Influences of warm eddies detached from the Kuroshio Extension, *J. Clim.*, *24*, 6551–6561.
Taguchi, B., S.-P. Xie, N. Schneider, M. Nonaka, H. Sasaki, and Y. Sasai (2007), Decadal variability of the Kuroshio Extension: Observations and an eddy-resolving model hindcast, *J. Clim.*, *20*, 2357–2377.
Tanimoto, Y., H. Nakamura, T. Kagimoto, and S. Yamane (2003), An active role of extratropical sea surface anomalies in determining anomalous turbulent heat flux, *J. Geophys. Res.*, *108*(C10), 3304, doi:10.1029/2002JC001750.
Tatebe, H., and I. Yasuda (2005), Interdecadal variations of the coastal Oyashio from the 1970s to the early 1990s, *Geophys. Res. Lett.*, *32*, L10613, doi:10.1029/2005GL022605.
Tomita, T., S.-P. Xie, and M. Nonaka (2002), Estimates of surface and subsurface forcing for decadal sea surface temperature variability in the mid-latitude North Pacific, *J. Meteorol. Soc. Jpn.*, *80*, 1289–1300.
Vivier, F., K. A. Kelly, and L. A. Thompson (2002), Heat budget in the Kuroshio Extension region: 1993-99, *J. Phys. Oceanogr.*, *32*, 3436–3454.
Wallace, J. M., and D. S. Gutzler (1981), Teleconnections in the geopotential height field during the Northern Hemisphere winter, *Mon. Weather Rev.*, *109*, 784–812.
Wu, R., and J. L. Kinter III (2010), Atmosphere-ocean relationship in the midlatitude North Pacific: Seasonal dependence and east-west contrast, *J. Geophys. Res.*, *115*, D06101, doi:10.1029/2009JD012579.
Wu, R., and B. P. Kirtman (2007), Regimes of seasonal air-sea interaction and implications for performance of forced simulations, *Clim. Dyn.*, *29*, 393–410.
Wu, R., B. P. Kirtman, and K. Pegion (2006), Local air-sea relationship in observations and model simulations, *J. Clim.*, *19*, 4914–4932.
Yamamoto, M., and N. Hirose (2011), Possible modification of atmospheric circulation over the northwestern Pacific induced by a small semi-enclosed ocean. *Geophys. Res. Lett.*, *38*, L03804, doi:10.1029/2010GL046214.

Yeh, S.-W., Y.-J. Kang, Y. Noh, and A. J. Miller (2011), The North Pacific climate transitions of the winters of 1976/77 and 1988/89, *J. Clim.*, *24*, 1170–1183.

Yu, L., X. Jin, and R. A. Weller (2008), Multidecade global datasets from the objectively analyzed air-sea fluxes (OAFlux) project: Latent and sensible heat fluxes, ocean evaporation, and related surface meteorological variables, *OAFlux Proj. Tech. Rep. OA-2008-01*, 64 pp., Woods Hole Oceanogr. Inst., Woods Hole, Mass.

Yulaeva, E., N. Schneider, D. W. Pierce, and T. P. Barnett (2001), Modeling of North Pacific climate variability forced by oceanic heat flux anomalies, *J. Clim.*, *14*, 4027–4046.